Schweizerische Eidgenossenschaft
Confédération suisse
Confederazione Svizzera
Confederaziun svizra

Eidgenössisches Departement für
Umwelt, Verkehr, Energie und Kommunikation UVEK

Bundesamt für Energie BFE

PARTIAL CATALYTIC OXIDATION OF CH_4 TO SYNTHESIS GAS FOR POWER GENERATION

Schlussbericht

Ausgearbeitet durch

Ioannis Mantzaras, Paul Scherrer Institute
CH-5232 Villigen PSI, ioannis.mantzaras@psi.ch, http://www.psi.ch

Adrian Schneider, Paul Scherrer Institute
CH-5232 Villigen PSI, adrian.schneider@psi.ch, http://www.psi.ch

Impressum

Datum: 13. März 2006

Im Auftrag des Bundesamt für Energie, Forschungsprogramm XY

Mühlestrasse 4, CH-3063 Ittigen

Postadresse: CH-3003 Bern

Tel. +41 31 322 56 11, Fax +41 31 323 25 00

www.bfe.admin.ch

BFE-Projektleiter: Bereichsleiter, bereichsleiter@bfe.admin.ch

Projektnummer: 47734

Bezugsort der Publikation: www.energieforschung.ch

Inhaltsverzeichnis

Zusammenfassung

Die partielle Oxidation von Methan zu Synthesegas über einem Rhodium-Katalysator wurde experimentell und numerisch im Druckbereich von 4 bis 10 bar untersucht. Das zugeführte Methan-Sauerstoff-Gemisch wurde mit grossen Mengen von H_2O und CO_2 verdünnt (bis zu 70 Vol.-Prozent), um neue Stromerzeugungs-Zyklen zu simulieren, welche mit einem hohen Grad von Abgas-Rückführung arbeiten. Experimente wurden in einem optisch zugänglichen Kanalströmungs-Reaktor durchgeführt, der in situ Messungen mit Lasermesstechniken erlaubt, sowie in einem massstäblich verkleinerten katalytischen Gasturbinen-Reaktor. Voll elliptische zweidimensionale numerische Codes für stationäre und transiente Fälle wurden benutzt. Sie enthalten chemische Reaktionsschemata für heterogene und homogene Elementarreaktionen. Die wesentlichen Ergebnisse sind die folgenden:

a) Heterogene (katalytische) und homogene (Gasphasen-) Reaktionsschemata wurden validiert für die partielle katalytische Oxidation von Methan mit einem hohen Grad von Abgasrückführung.

b) Die Auswirkungen von zugefügtem H_2O und CO_2 wurden aufgeklärt. Das zugefügte H_2O erhöhte den Grad der Methan-Umsetzung und die Selektivität für Wasserstoff, während die CO-Selektivität vermindert wurde. Die Auswirkungen von zugefügtem CO_2 auf die Chemie (trockene Reformierung) waren minimal.

c) Das numerische Modell reproduzierte die gemessenen katalytischen Zündzeiten. Des weiteren wurde gezeigt, dass die chemische Auswirkung von H_2O und CO_2 auf die katalytischen Zündverzugszeiten minimal war.

d) Die Dispersion des Edelmetalls nahm mit verschiedenen Trägermaterialien zu, und zwar in der Reihenfolge Rh/α-Al_2O_3, Rh/ZrO_2, und Rh/Ce-ZrO_2. Es wurde eine offensichtliche Beziehung zwischen der Dispersion des Edelmetalls und dem katalytischen Verhalten gefunden.

Abstract

The partial oxidation of methane to synthesis gas over rhodium catalysts has been investigated experimentally and numerically in the pressure range of 4 to 10 bar. The methane/oxidizer feed has been diluted with large amounts of H_2O and CO_2 (up to 70% vol.) in order to simulate new power generation cycles with large exhaust gas recycle. Experiments were carried out in an optically accessible channel-flow reactor that facilitated laser-based in situ measurements, and also in a subscale gas-turbine catalytic reactor. Full-elliptic steady and transient two-dimensional numerical codes were used, which included elementary hetero-/homogeneous chemical reaction schemes. The following are the key conclusions:

a) Heterogeneous (catalytic) and homogeneous (gas-phase) schemes have been validated for the partial catalytic oxidation of methane with large exhaust gas recycle.

b) The impact of added H_2O and CO_2 has been elucidated. The added H_2O increased the methane conversion and hydrogen selectivity, while it decreased the CO selectivity. The chemical impact of CO_2 (dry reforming) was minimal.

c) The numerical model reproduced the measured catalytic ignition times. It was further shown that the chemical impact of H_2O and CO_2 on the catalytic ignition delay times was minimal.

d) The noble metal dispersion increased with different support materials, in the order Rh/α-Al_2O_3, Rh/ZrO_2, and Rh/Ce-ZrO_2. An evident relationship was established between the noble metal dispersion and the catalytic behavior.

1. Ausgangslage

The initial conditions as well as the required new developments in both the experimental and numerical sides are summarized below.

a.1) existing experimental infrastructure

An optically accessible channel-flow reactor was already available at the Combustion Fundamentals Group (CFG) of PSI. In addition, a steam-generator unit (used to simulate the exhaust gas recycle) had been constructed via a previous KTI project on fuel-lean catalytic combustion. From the laser-based measuring techniques, the spontaneous Raman scattering was already established in earlier studies by the Combustion Diagnostics group of PSI.

a.2) new experimental infrastructure

The infrastructure necessary to accommodate experiments with the subscale gas-turbine catalytic reactor was built in the present project. In addition, two new measuring techniques were established. Firstly, laser induced fluorescence (LIF) of formaldehyde was developed by the Combustion Diagnostics group to monitor gas-phase combustion in the optically accessible reactor. Secondly, gas-chromatography was advanced at the Combustion Fundamentals Group to facilitate exhaust gas analysis measurements in the subscale gas-turbine reactor.

b.1) existing numerical tools

In the numerical front, a 2D steady elliptic code with detailed heterogeneous and homogeneous chemical reaction schemes was already available at CFG. The code was an in-house development, continuously upgraded during the period 1997-2003.

b.2) new numerical tools

The steady code has been extended to transient, in order to simulate catalytic ignition.

2. Ziel der Arbeit

The goals set in the project were:

a) To establish reliable heterogeneous and homogeneous chemical reaction schemes that reproduce the measured ignition characteristics in partial catalytic oxidation of methane. The heterogeneous ignition (catalytic ignition or light-off) is crucial in gas-turbines of power generation systems due to the stringent demands for reactor inlet temperatures less than 700 K. On the other hand, the homogeneous (gas-phase) ignition is detrimental to the catalyst integrity and thus the availability of validated numerical models is imperative for safety considerations during reactor design.

b) To understand the impact of large exhaust gas recycle (EGR), i.e. H_2O and CO_2 dilution, on the steady reactor performance (methane conversion, reactor temperature, synthesis gas yields and selectivities). Moreover, to study the impact of dilution on the heterogeneous ignition characteristics (light-off times).

c) To evaluate the effect of pressure on key reactor performace parameters such as methane conversion and synthesis gas yields and selectivities in partial oxidation with large EGR.

d) To screen different catalysts and to determine catalyst formulas suitable for patial oxidation of methane in power generation systems. For a given noble metal catalyst, to further investigate the effect of support.

e) To address thermal management issues (maximum tolerable temperatures) in reactors used for power generation.

3. Methodologie

3.1 Experimental

3.1.1 Optically accessible catalytic channel-flow reactor

Experiments were carried out in an optically accessible catalytic channel-flow reactor, positioned inside a high-pressure cylindrical tank (Fig. 1). The reactor comprised two non-porous Si[SiC] ceramic plates (300 mm long, 104 mm wide, placed 7 mm apart) and two 3-mm-thick quartz windows. A Rh/ZrO_2 coating was applied to the inner Si[SiC] surfaces. The surface temperatures were monitored by thermocouples (twelve for each plate) arranged along the *x*-*y* symmetry plane and embedded 0.9 mm beneath the catalyst through holes eroded from the outer Si[SiC] surfaces. Two 350-mm-long and 35-mm-thick quartz windows on the high-pressure tank maintained optical access from both reactor sides. Two additional quartz windows, one at the rear flange of the tank and the other at the reactor exit (Fig. 1a), provided a further streamwise optical access for the LIF excitation beam. Details of the reactor/tank assembly have been provided in earlier publications [1, 2].

Oxygen was provided from high-pressure bottles and nitrogen served as balance. Superheated steam was supplied by an AWTEC-DLR steam-generator (Fig. 1c). The device comprised a H_2/O_2 preburner that further ignited a main H_2/O_2 burner, the latter being operated slightly fuel-lean through the feedback control of a lambda probe. The combustion heat was in turn used to vaporize accurately-measured amounts of demineralized liquid water. A Ni/Pd catalyst positioned downstream the main burner served as a safety backup to convert any escaping hydrogen and to assure high degree of steam purity.

The O_2, N_2 and CO_2 flows were mixed and then electrically preheated. Room-temperature CH_4 and superheated steam were injected downstream; the feed achieved a good degree of premixedness in two sequential static mixers and a 30-mm-long packing of 2-mm-diameter ceramic spheres. The mixture was finally driven into the reactor through a 50-mm-long inert honeycomb. A thermocouple positioned at the downstream end of the honeycomb provided the inlet temperature of the feed.

3.1.2 Laser diagnostics

The Raman/LIF set-up, along with its arrangement in the optically accessible reactor, is depicted in Fig. 2. A traversable mirror directed the frequency-doubled 532 nm radiation of an Nd:YAG pulsed laser (Quantel YG981E20-CL, 380 mJ pulse energy, 12 ns pulse) to the Raman or to the LIF set-up. In the Raman experiments, the 532 nm beam was temporally stretched to 34 ns using a partially reflecting mirror and an optical delay line for the transmitted radiation (Fig. 2). This allowed for efficient use of the entire pulse energy without window damage or dielectric gas breakdown. The temporally-stretched and expanded (25 mm diameter) beam was focused through the tank and reactor side-windows into a vertical line (~0.3 mm thick) by an f_1 = 150 mm cylindrical lens. The focal line spanned the 7-mm transverse gap and was laterally offset (z = 15 mm) to increase the light collection angle and minimize thermal beam steering [3, 4]. Two f_2 = 300 mm spherical lenses focused the scattered light to the entrance slit of a 25 cm imaging spectrograph (Chromex-250i). The dispersed light was recorded on an intensified CCD camera (Princeton Instruments MAX-1024HQ, 1024x254 pixels). To increase the spatial resolution, only the upper channel half-height was recorded. Each image comprised 630x254 pixels that corresponded to wavelength and transverse (y) distance, respectively. The 3.5 mm half-height was resolved with 200 pixels, which were further binned to 84 pixels. A holographic notch-filter (Kaiser HNPF-532.0-1.5) and a colored glass filter were placed before the spectrograph slit to attenuate the scattered Rayleigh signal and the stray laser light. The spectral dispersion extended up to 4500 cm^{-1}, allowing observation of all major species. Given the steady operating conditions, 2000 images were averaged to increase the signal-to-noise ratio. The effective Raman cross-sections were evaluated by recording the signals of several pressurized CH_4, N_2/H_2 and CO_2 containing mixtures, air, and the actual feed mixture. Those tests also quantified the cross-talk between the CO_2/O_2 and CO/N_2. Spectroscopic data for the CH_4, H_2O, CO_2 and CO Raman cross-sections were obtained from Refs. [5-7]. Measurements were acquired at 14 mm $\leq x \leq$ 168 mm by traversing axially an optical table that supported both sending and collecting optics (Fig. 2). Raman data closer than 0.3 mm to the upper wall were discarded due to low signal-to-noise ratio.

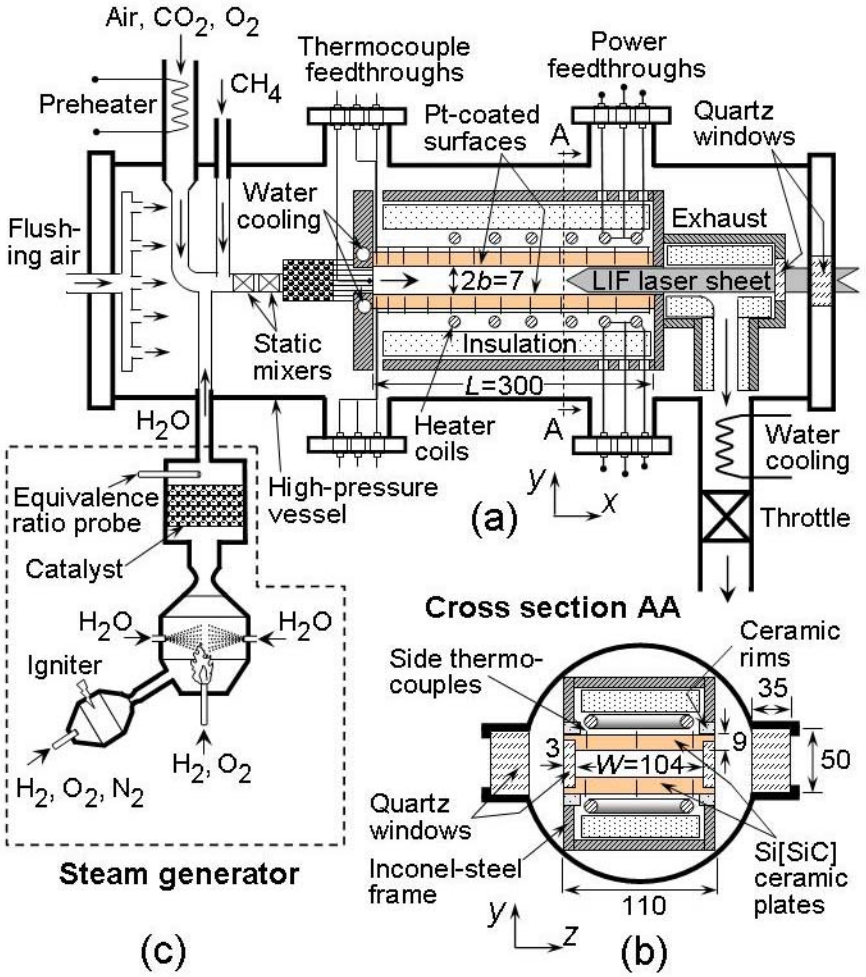

Figure 1: *Test rig for optically accessible reactor (a, b) and steam generator (c). All lengths are in mm.*

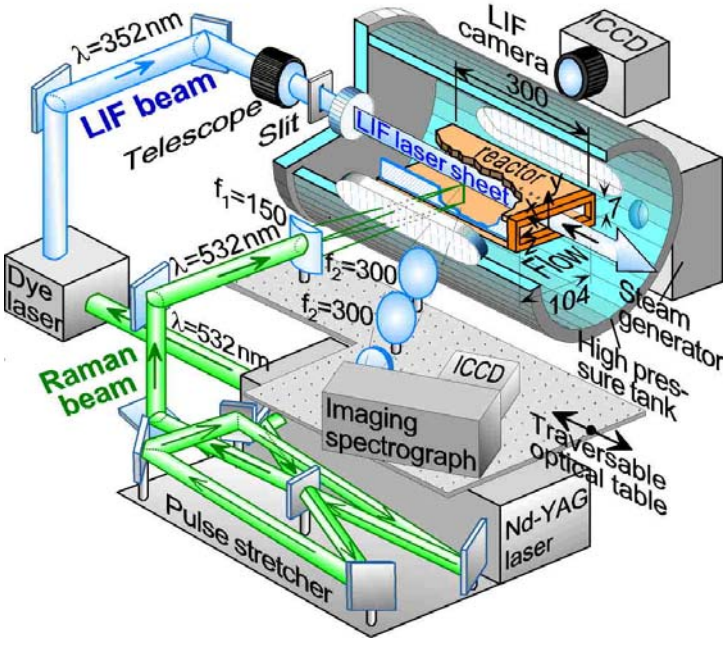

Figure 2: *Optical setup for Raman and LIF. All focal lengths are in mm.*

At fuel-rich conditions, planar LIF of OH was not amenable due to the associated sub-ppm levels [2]. Formaldehyde LIF was thus introduced, whereby the 532 nm radiation pumped a tuneable dye laser (Quantel TDL90 NBP2UVT3) filled with pyridine-1 dye. Its frequency-doubled radiation at 352 nm was transformed into a slightly diverging laser sheet (propagating counterflow along the *x*-*y* symmetry plane, Fig. 2) by a telescopic system. The broadband fluorescence was collected at 90° with an intensified CCD camera (LaVision-IRO with 1392x1024 pixels, recorded with a binning of 2x2). The collection optics included achromatic lenses and filters that provided spectral detection between 410 and 480 nm. Zones of 110x7 mm^2 were recorded on a 696x44 pixel section, and the camera was traversed axially to map the entire reactor extent. The present study reports the first direct measurements of homogeneous ignition in CPO using CH_2O-LIF. In catalytic systems, this technique has only been used to measure the pure heterogeneous production of formaldehyde in the oxidation of methanol over Pt [8] at low temperatures (140°C).

3.1.3 Accuracy of the laser-based measurements

The Raman measurement accuracy was ±3% for species compositions ≥ 10% vol. and ±10% for compositions as low as 0.5% vol.; concentrations less than 0.5% vol. entailed larger measurement uncertainties.

Uncertainties in the broadband emission of formaldehyde and the significant laser radiation absorption along its propagation path (given the large amounts of CH_2O) precluded quantification of the LIF signals. However, since the LIF data were used only to determine the spatial location of homogeneous ignition, absolute concentration measurements of formaldehyde were not necessary.

3.1.4 Subscale gas-turbine honeycomb reactor

The short contact time honeycomb catalytic reactor constituted a subscale unit of a prototype burner developed for large gas turbines of power generation systems [9] and formed a liner inside a high-pressure tank (Fig. 3a). The same subscale reactor geometry has also been used in earlier CH_4/air catalytic combustion studies, which included complete oxidation over Pd [10] and partial oxidation over Rh/ZrO_2 [11]. It comprised a 35 mm inner-diameter and 1.5 mm thick steel tube, wherein alternating flat and corrugated 50-μm-thick FeCr-alloy foils created a honeycomb structure with individual channel hydraulic diameters of d_h = 1.2 mm (see Fig. 4). The reactor had a total length L = 75 mm and was mounted inside a well-insulated (with a 30-mm-thick fiber ceramic) cylindrical steel frame. Only the central reactor extent (L_c = 55 mm) was coated with a catalyst, while both end-sections with corresponding lengths L_u = 10 mm were catalytically inactive (Fig. 3a). The inlet, outlet and reactor temperatures were monitored with five 50-μm-thick K-type (Ni/Cr-Ni/Al) sheathed thermocouples. The thermocouple beads were positioned at x = -15, 0, 27, 55 mm and 75 mm (x = 0 denotes the beginning of the catalytically active section). The carrying wires of the four thermocouples *A* to *D* (Fig. 3a) were driven counterflow into the reactor through four honeycomb channels. The three thermocouples inside the honeycomb structure (*B*, *C* and *D*) provided neither the true surface temperature nor the mean gas temperature but rather a weighted average, which was only indicative of the local temperature.

The steam generator (described in the foregoing Section 3.1.1) supplied superheated steam. High-pressure bottles supplied CO_2, O_2, and technical-grade CH_4 (> 99.5%). Three Brooks mass-flow controllers regulated the flows of those gases, leading to equivalence ratio accuracies better than ±0.5%. The CO_2 and O_2 flows were preheated by a 3 kW resistive heater and then mixed with superheated steam and room-temperature methane (see Fig. 3a) in two sequential static mixers (Sulzer SMV). A follow-up 40-mm-long packing of 2-mm-diameter ceramic spheres straightened the flow. A K-type thermocouple positioned downstream of the static mixers monitored the gas temperature, which was then used to control the level of CO_2/O_2 preheat and the degree of steam superheat. The honeycomb was affixed 8 mm downstream of the flow straightener, and was mounted inside a 2.5 mm thick and 35 mm internal diameter holder steel tube. To further minimize heat losses, only the first and last 2 mm of the honeycomb contacted the holder tube, while in the remaining length a 1-mm-thick annular air-cushion was available. Finally, a discharge nozzle at the end of the holder tube directed the flue gases first to an exhaust pipe and then to a water-cooled outlet of the high pressure tank.

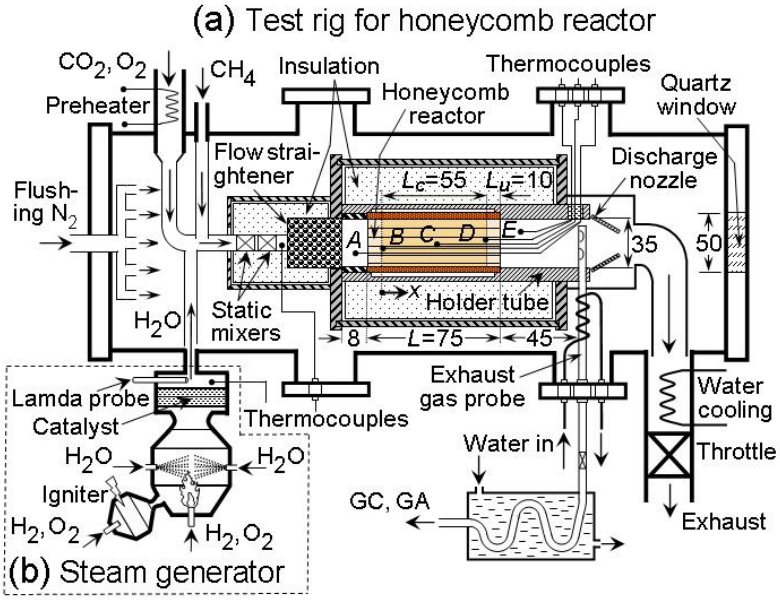

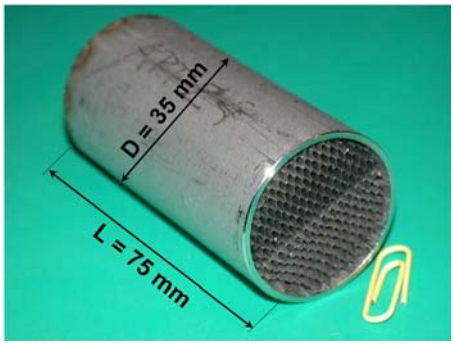

Figure 3: *Test rig for subscale gas-turbine honeycomb reactor. All lengths are in mm.*

Figure 4: *Photograph of subscale catalytic gas-turbine honeycomb reactor.*

The high pressure tank that housed the reactor was the same stainless-steel cylindrical structure described in Section 3.1.1. For safety reasons the flue gases were diluted with flushing nitrogen, which flowed continuously in the free volume between the high pressure tank and the reactor. Visual inspection of the reactor assembly was achieved via a quartz window at the rear flange of the tank (Fig. 3a) and two 350-mm-long quartz windows at the tank sides (discussed within the context of the optically accessible reactor in Fig. 1b). The gas sampling probe with its associated water cooling lines (see Section 3.1.5) and the thermocouple wires were driven inside the tank through high-pressure fittings mounted on four dedicated flanges.

3.1.5 Gas analysis

The exhaust gas was sampled with a water-cooled, silica-coated steel probe positioned 45 mm downstream of the honeycomb (Fig. 3a). The steam of the sampled gas was condensed in a water-cooled serpentine heat exchanger outside the high pressure tank. The dried gases entered a rack of gas analyzers (GA) and the sample port of a gas chromatograph (GC). Removal of the large steam content was necessary for the proper operation of both analysis instruments. Nonetheless, the compositions of the actual wet gas products could be determined by calculating the element balances.

The Hartmann and Braun gas analyzers Uras-10E for CO (NDIR), Magnos-6G for O_2 (paramagnetic) and Caldos-5G for H_2 (thermal-conductivity-based) were used in a continuous analysis mode. The accuracy of the GA measurements has been determined with calibration gas mixtures and was particularly good for CO (0.3% relative error for 10-14% vol. CO in the dry gas); the accuracy of O_2 was still good despite its associated low levels (20% relative error for ~1% vol. O_2). The presence of gases with thermal conductivities considerably different than that of the reference nitrogen (e.g. CH_4 and CO_2) resulted in larger inaccuracies for hydrogen (20% relative error for typical ~30% vol. H_2 in the dry gas); this effect was partly compensated by calibrating the device with simulated exhaust gas compositions. In parallel to the GA measurements, more detailed analysis was carried out in an HP-6890++ GC equipped with porous polymer and molecular sieve columns and a thermal conductivity sensor. The porous polymer column separated CO_2 before the gas entered the molecular sieve. Helium was the carrier gas, while the analysis was discontinuous with one measurement every 8 min. The GC has been tested against a selection of different calibration gas mixtures.

3.1.6 Accuracy of the gas-chromatography and temperature measurements

Even though the hydrogen signals were weak due to the choice of helium as carrier gas, for the substantial amounts of the present work (~30% vol. H_2) the accuracy was good (~4% relative error for H_2). The relative error in the GC measurements was 4-5% for CH_4, CO_2 and CO, increasing up to 50% for the scarce O_2. In the forthcoming sections only the GC measurements will be presented; the GA data have provided an additional (and successful) control mainly for the GC-measured CO and O_2 compositions.

Of the two measured true local gas temperatures (*A*, *E* in Fig. 3a), radiation corrections (amounting up to 8 K) have been applied to the inlet thermocouple (*A*) that had a direct view to the hot catalyst entry; no such corrections were required for the outlet thermocouple (*E*) due to the small difference between the exit gas and rear reactor wall temperature (~20°C). The absolute accuracy of the gas temperature measurements was ±10 K for the hot outlet and ±6 K for the inlet.

3.1.7 Catalyst preparation and characterization

Three support materials were investigated in the honeycomb reactor, Ce-ZrO_2 (17.5 wt% CeO_2), ZrO_2, and α-Al_2O_3. The basic experiments in the two reactors were carried out with the Rh/ZrO_2 catalyst. The other supports were examined in some detail in a separate screening study. The supports had previously been calcined at 1373 K for 10 h (Al_2O_3) or 1073 K for 5 h (Ce-ZrO_2 and ZrO_2). The catalysts, containing 1 %wt. Rh, were prepared by incipient wetness impregnation using aqueous solutions of $Rh(NO_3)_3$. The impregnated supports were dried at 383 K, followed by calcination at 873 K for 5 h. A slurry, obtained by ball-milling the catalyst powder in a solvent mixture for 24 h, was sprayed on the FeCr-alloy foils of the honeycomb reactor and on the Si[SiC] plates of the channel-flow reactor; the coated structures were further calcined at 873 K for 1 h. The resulting catalyst layer had a thickness (δ_c) of 4.6 □m. Before a combustion run −in either reactor configuration− the catalyst was reduced in a heated (673 K) H_2/N_2 flow for 15 min.

The total and active areas of the catalysts were measured with BET (N_2-physisorption) and H_2-chemisorption, respectively. The total surface area of fresh catalyst powder samples was determined by nitrogen adsorption at liquid nitrogen temperature using a Micromeritics ASAP 2010 instrument. All samples were degassed at 523 K prior to analysis. The surface area was calculated according to the method of Brunauer, Emmett and Teller (BET). Hydrogen chemisorption analysis was performed on a Quantachrome Autosorb-1C to determine the noble metal dispersion of the tested catalyst samples. The samples were reduced in H_2 (50 ml/min) at 673 K for 1 h followed by evacuation (673 K for 1 h) prior to the analysis. The adsorption measurements were performed at 195 K using hydrogen and considering a H_2:Rh stoichiometry of 1:2. The adsorption temperature of 195 K was selected in order to suppress spill-over of hydrogen to the support, which has been reported to occur for ceria-containing support materials under certain conditions [12]. The metal dispersion was calculated according to the dual isotherm method.

The crystal structure of the support materials was investigated with a confocal Raman microscope (Labram, DILOR) equipped with a 100 × magnification objective (laser spot size 0.1 μm) and a thermoelectrically cooled CCD detector (1152×300 pixels). The Raman spectra were obtained in a backscatter mode with the 632.8 nm line of a He-Ne laser that yielded a power of ~4 mW at the sample surface. Raman spectra were recorded in the range from 100 to 1100 cm^{-1} using an 1800 grooves/mm grating. The lateral resolution of the Raman microscope was about 2 μm.

The measured active surface area was also a parameter needed in the numerical model. Although hydrogen chemisorption tests have been carried out only on powders recovered from tested FeCr-alloy foils (testing on the large-sized coated Si[SiC] plates required their mechanical destruction), the active area of the Si[SiC] plates was considered equal to that of the FeCr foils. This was a good approximation given the non-porous nature of both FeCr and Si[SiC] surfaces; moreover, this was also supported by BET/chemisorption tests of fragmented Pt-coated Si[SiC] plates in earlier total oxidation studies [4].

3.2 Numerical

A steady and an unsteady, two-dimensional, full elliptic laminar numerical code was used that included detailed hetero-/homogeneous chemistry and transport, as well as heat transfer mechanisms in the solid. A single-channel model has been considered for the honeycomb reactor, which was an adequate approach given the good thermal insulation and the uniform inlet properties at the entry face of the reactor. Each channel was modeled as an equivalent cylindrical tube with a radius r_h = 0.6 mm. The same numerical code was also used to simulate the channel-flow experiments; therein, Cartesian coordinates were used [3] to model the reactive flow along the *x*-*y* plane of symmetry (*L*x2*b* in Fig. 1).

3.2.1 Subscale gas turbine honeycomb channel

Details are provided below for the unsteady channel simulations. Given the good thermal insulation and the uniform properties at the front face of the honeycomb a single-channel model has been constructed. A full elliptic 2-D quasisteady model was employed for the reactive gas flow. On the other hand, the spatial dimensionality of the solid was dictated by characteristic time considerations. The characteristic time for axial convection was $t_{g,x}$ ~ (9-12)x10^{-3} s, while for radial gas diffusion the characteristic time (r_h^2/α_g) was $t_{g,r}$ ~ (5-20)x10^{-3} s (using gas properties in the range 680 to 1180 K). The corresponding times for solid heat conduction, axial ($L^2/\alpha_{\mathrm{FeCr}}$) and radial [$(\delta/2)^2/\alpha_{\mathrm{FeCr}} + \delta_c^2/\alpha_{\mathrm{ZrO2}}$], were $t_{s,x}$ ~ (1.6-2.4)x10^3 s and $t_{s,r}$ ~ (0.3-0.4) x10^{-3} s, respectively. Since the equilibration of the gas required times at least as long as $t_{g,r}$, the significantly faster radial solid heat conduction could not be resolved within the gas-phase quasisteady assumption. This condition was typical to many practical systems, whereby the high pressures led to elongated gas diffusion times. Thus, a 1-D approach for the solid has been adopted. A step of 50 ms, sufficiently long for gas-phase equilibration, was used for time integration.

Governing equations

For a quasisteady laminar channel-flow with hetero-/homogeneous reactions, the governing equations in cylindrical coordinates become:

Continuity:

$$\frac{\partial(\rho u)}{\partial x}+\frac{1}{r}\frac{\partial(r\rho v)}{\partial r}=0\,. \tag{1}$$

Axial momentum:

$$\frac{\partial(\rho uu)}{\partial x}+\frac{1}{r}\frac{\partial(r\rho vu)}{\partial r}=-\frac{\partial p}{\partial x}+\frac{\partial}{\partial x}\left[2\mu\frac{\partial u}{\partial x}-\frac{2}{3}\mu\left(\frac{\partial u}{\partial x}+\frac{1}{r}\frac{\partial(rv)}{\partial r}\right)\right]+ +\frac{1}{r}\frac{\partial}{\partial r}\left[\mu r\left(\frac{\partial u}{\partial r}+\frac{\partial v}{\partial x}\right)\right]. \tag{2}$$

Radial momentum:

$$\frac{\partial(\rho uv)}{\partial x}+\frac{1}{r}\frac{\partial(r\rho vv)}{\partial r}=-\frac{\partial p}{\partial r}+\frac{\partial}{\partial x}\left[\mu\left(\frac{\partial v}{\partial x}+\frac{\partial u}{\partial r}\right)\right]+\frac{\partial}{\partial r}\left[2\mu\frac{\partial v}{\partial r}-\frac{2}{3}\mu\left(\frac{\partial u}{\partial x}+\frac{1}{r}\frac{\partial(rv)}{\partial r}\right)\right]+ +\frac{2\mu}{r}\left(\frac{\partial v}{\partial r}-\frac{v}{r}\right). \tag{3}$$

Total enthalpy:

$$\frac{\partial(\rho uh)}{\partial x}+\frac{\partial(r\rho vh)}{\partial r}=\frac{\partial}{\partial x}\left(\lambda_g\frac{\partial T}{\partial x}-\rho\sum_{k=1}^{Kg}Y_k h_k V_{k,x}\right)+\frac{1}{r}\frac{\partial}{\partial r}\left(r\lambda_g\frac{\partial T}{\partial r}-r\rho\sum_{k=1}^{Kg}Y_k h_k V_{k,r}\right). \tag{4}$$

Gas-phase species:

$$\frac{\partial(\rho uY_k)}{\partial x}+\frac{1}{r}\frac{\partial(r\rho vY_k)}{\partial r}=-\frac{\partial}{\partial x}\left(\rho Y_k V_{k,x}\right)-\frac{1}{r}\frac{\partial}{\partial r}\left(r\rho Y_k V_{k,r}\right)+\dot{\omega}_k W_k\,,\quad k = 1,..,\, K_g. \tag{5}$$

Surface species coverage:

$$\frac{\partial \theta_m}{\partial t} = \sigma_m \frac{\dot{s}_m}{\Gamma}, \quad m = 1,.., M_s. \tag{6}$$

The left side of Eqs. (6) was not a true transient term and its inclusion merely facilitated convergence to steady state. The diffusion velocities were computed using mixture-average plus thermal diffusion for the light species [13]:

$$\vec{V}_k = -(D_{km} / Y_k)\nabla Y_k + (D_k^T / \rho Y_k T)\,\nabla T, \quad k = 1,.., K_g. \tag{7}$$

Finally, the ideal gas and caloric state laws were:

$$p = \frac{\rho R T}{\overline{W}} \text{ and } h_k = h_k^{\circ}(T_{\circ}) + \int_{T_{\circ}}^{T} c_{p,k}\, dT \text{, with } h = \sum_{k=1}^{Kg} Y_k h_k, \quad k = 1,.., K_g. \tag{8}$$

The time-dependent energy balance for the 1-D solid was:

$$\left[\rho_{\mathrm{FeCr}} \frac{\partial (c_{\mathrm{FeCr}} T_W)}{\partial t} - \lambda_{\mathrm{FeCr}} \frac{\partial^2 T_W}{\partial x^2}\right]\frac{\delta}{2} - \left[\dot{q}_{\mathrm{rad}} - \lambda_g \left.\frac{\partial T}{\partial r}\right|_{r=r_h-} + B\sum_{k=1}^{Kg}\left(\dot{s}_k h_k W_k\right)_{r=r_h}\right]\left(\frac{2r_h}{2r_h + \delta/2}\right) = 0 \tag{9}$$

The solid thickness in Eq. (9) corresponded to half of the FeCr-alloy ($\delta/2$ = 25 μm) due to the consideration of adjacent channels. The thinner catalyst layer (δ_c = 4.6 μm) was neglected since its thermal conductivity and thermal inertia ($\rho_{\mathrm{ZrO2}} c_{\mathrm{ZrO2}}\, \delta_c$) were at least an order of magnitude lower than those of the FeCr-alloy, irrespective of temperature. For the FeCr-alloy, a temperature-dependent heat capacity was considered while the thermal conductivity was taken constant at its 300 K value of 16 W/mK. The net received radiant heat flux ($\dot{q}_{\mathrm{rad}}$ in Eq. (9)) accounted for the radiation exchange of each differential cylindrical surface element with all other differential surface elements as well as with the channel entry and outlet, and was modeled by the net radiation method for diffuse-gray areas [14]. Details of the radiation model have been provided elsewhere [15]. The emissivities of all differential channel elements were equal to ε = 0.6, while the inlet and the outlet sections were treated as black bodies (ε = 1.0). The radiation exchange temperatures for the entry and outlet were considered equal to the corresponding mean gas temperatures. It will be shown, however, that radiation effects were altogether minimal.

Boundary conditions and method of solution

The gas-phase species interfacial boundary conditions were:

$$(\rho Y_k V_{k,r})_{r=r_h-} + B\,\dot{s}_k W_k = 0, \quad k = 1,.., K_g, \tag{10}$$

with $\dot{s}_k = 0$ over the inactive channel length. The factor *B* in Eqs. (9) and (10) was the ratio of the active to the geometrical surface area and has been determined by H_2 chemisorption. Those tests provided the active areas in m^2/gr-Rh for the used catalysts; with known size, weight and noble metal content of the analyzed samples, the values of *B* could be calculated. It is noted that the fresh samples had considerably higher measured *B* factors as they comprised both high-surface-area tetragonal phase and low-surface-area monoclinic ZrO_2 phase (detected with surface Raman measurements), while the used samples comprised only monoclinic phase [16]. The *B* values of the used samples were maintained in successive combustion runs and were, therefore, employed in the ensuing simulations. Intraphase species diffusion was not considered since the catalyst layer was only 4.6 μm thick and was applied on a non-porous FeCr-alloy.

Radiative boundary conditions were applied at the reactor inlet and outlet:

$$\lambda_{\mathrm{FeCr}}\, \partial T_W / \partial x = \varepsilon\sigma\,[T_W^4(x) - T_{\mathrm{IN}}^4] \qquad \text{at } x = -L_u$$

$$-\lambda_{\mathrm{FeCr}}\, \partial T_W / \partial x = \varepsilon\sigma\,[T_W^4(x) - T_{\mathrm{OUT}}^4] \qquad \text{at } x = L_c + L_u. \tag{11}$$

Uniform profiles for the axial velocity, the species mass fractions and the temperature were specified at the inlet. The 8 mm gap between the flow straightener and the honeycomb entry created only a very thin boundary layer (less than 0.4 mm thick, since the Reynolds numbers in the 35 mm diameter holder tube exceeded 15,000), thus justifying the consideration of a single representative channel with a constant inlet velocity. At the symmetry axis ($r = 0$) and the outlet ($x = L_c + L_u$) zero-Neumann boundary conditions were applied for all thermoscalars and the axial velocity.

The coupled set of flow and solid equations (Eqs. (1) to (6) and Eq. (9)) were solved simultaneously. A finite volume scheme was adopted for the spatial discretization of the flow equations and solution was obtained with a SIMPLER method for the pressure-velocity field [17]; details on the quasisteady flow solution have been provided elsewhere [18, 19]. For the transient solid equation, a second order accurate, fully implicit scheme was constructed by using a quadratic backward time discretization [20]. At a given time step, the coupled flow and solid phases were solved iteratively such that at convergence the solid temperature did not vary by more than 10^{-4} K. An orthogonal staggered grid of 220x24 points in x and r, respectively, (75 mm x 0.6 mm) with finer axial spacing towards the start of the catalytic section and radial spacing closer to the wall, was sufficient to produce a grid-independent solution; the axial discretizations in the solid and gas were the same (220 points). For time integration, the step was $\Delta t = 50$ ms. The CPU time for a 10-sec-long integration was ~15 h on a 2.6 GHz Opteron processor when gas chemistry was not included (otherwise the CPU time increased by a factor of four). Finally, a cluster of twenty same processors was used for elaborate parametric studies.

3.2.2 Channel-flow reactor

The interfacial energy boundary conditions ($y = 0$ and $y = 2b$) in the optically accessible channel-flow reactor were substantially simpler, given the direct measurement of the surface temperatures. The species and energy interfacial boundary conditions were:

$$(\rho Y_k V_{k,y})_{y=0} = BW_k(\dot{s}_k)_{y=0}, \quad -(\rho Y_k V_{k,y})_{y=2b} = BW_k(\dot{s}_k)_{y=2b} \tag{12}$$

and

$$T(x, y=0) = T_{W,L}(x), \quad T(x, y=2b) = T_{W,U}(x), \tag{13}$$

with $T_{W,U}(x)$ and $T_{W,L}(x)$ the measured temperatures of the upper and lower wall, respectively.

3.2.3. Chemical Kinetics

The detailed heterogeneous reaction mechanism of Deutschmann (Schwiedernoch et al. [21]) was used for CPO of methane over rhodium (38 reactions, 12 surface and 6 gas species). Fundamental kinetic studies in the optically accessible reactor of Fig. 1 have shown that this scheme reproduced the methane conversion and synthesis gas yields in CPO of CH_4/air [2] and $CH_4/O_2/H_2O/CO_2$ [22] over Rh/ZrO_2 catalysts. The surface site density was $\Gamma = 2.72 \times 10^{-9}$ mol/cm^2.

The C_2/H/O homogeneous reaction mechanism of Warnatz et al. [23] was used to assess the effect of gaseous chemistry (164 reversible reactions and 34 species). This reaction scheme has been shown to capture the onset of homogeneous ignition in the aforementioned studies [2, 22]. However, simulations of the present honeycomb experiments with the above hetero-/homogeneous mechanisms have shown that gas-phase chemistry was insignificant. The gaseous chemistry had also a negligible contribution over the 45-mm-long gap separating the reactor exit and the sampling probe (Fig. 3), as shown by additional plug-flow-reactor simulations. The negligible gas-phase chemistry contribution was further verified experimentally. Turning the cooling water of the sampling probe off, led to only 3% relative rise in the GC-measured hydrogen volumetric composition, even though the residence time in the visibly hot section of the probe was nearly ten times longer than that of the reactor. Therefore, the gaseous chemistry was not included in the honeycomb simulations.

The CHEMKIN database was used to evaluate transport properties [13]. Thermodynamic data for the gas-phase species were included in the gas-phase chemical scheme. Finally, surface and gas-phase reaction rates were evaluated with SURFACE CHEMKIN [24] and CHEMKIN [25], respectively.

4. Ergebnisse

Results are presented in four areas, a) Validation of hetero-/homogeneous chemical reaction schemes, b) Impact of H_2O and CO_2 dilution on steady catalytic partial oxidation (CPO), c) transient light-off and d) catalyst screening for selection of appropriate catalysts for CPO with large EGR. The following results have been summarized in the publications with Refs. [11,16,22,28].

4.1 Validation of hetero-/homogeneous chemical reaction schemes.

4.1.1 Heterogeneous processes

Comparisons between Raman-measured and predicted species transverse profiles are illustrated in Figs. 5 and 6 for two selected cases of Table 1. For clarity, up to 20 of the total 84 measuring points are provided over the experimentally resolved extent $0 \leq y \leq 3.2$ mm. Gas-phase chemistry was negligible at $x \leq 120$ mm (Fig. 5) and $x \leq 86$ mm (Fig. 6), wherein its contribution was less than ~5% of the catalytic pathway. Those axial extents corresponded to the first four transverse profiles of Fig. 5 and the first three profiles of Fig. 6.

Case	p (bar)	φ	T_{IN} (K)	U_{IN} (m/s)	CH_4	H_2O	CO_2
1	4	2.5	457	1.72	20	42	-
2	6	4.0	566	1.62	29	38	-
3	8	2.5	569	1.07	20	43	*20*
4	10	2.5	553	0.82	21	42	*21*
5	10	4.0	549	0.93	30	37	-

Table 1: *Experimental conditions in optically accessible reactor. Inlet properties and %vol. feed composition. Case 1 has also 22% vol. CO. The O_2 is deduced from the equivalence ratio (φ) and the balance is N_2.*

The predicted onset of homogeneous ignition (defined in the next section by the formaldehyde rise) was located ~20 mm farther downstream of the aforementioned onset of appreciable gas-phase contribution. Over this extent, comparisons between measured and predicted methane mole fractions indicated relative differences of up to 4% (see Figs. 5 and 6), which were well-within the experimental uncertainty.

In the H_2O dilution cases, the partial oxidation products (CO and H_2) were somewhat underpredicted (Figs. 5(d, e), 6(c,d)). On the other hand, the total oxidation products (CO_2 and H_2O) were slightly overpredicted as shown in Fig. 5 (CO_2 and H_2O are not provided in Fig. 6, however, the same trends were also observed there). Thus, the employed heterogeneous reaction scheme favored slightly the total over the partial oxidation route.

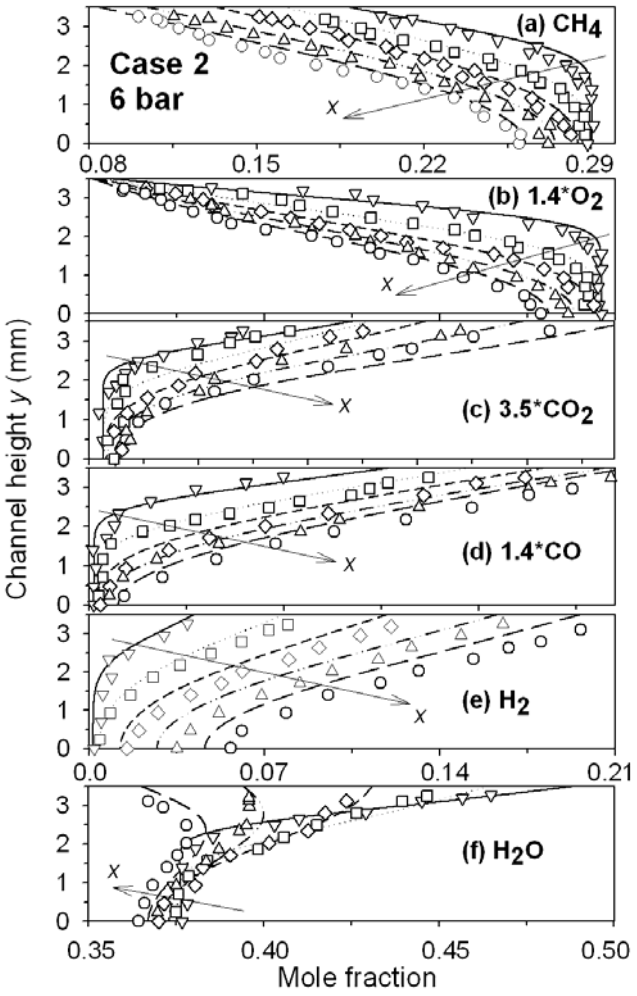

Figure 5: *Predicted (lines) and measured (symbols) profiles of species mole-fraction for Case 2:* x=*14mm (solid-lines, lower-triangles),* x=*48mm (dotted-lines, squares),* x=*88mm (short-dashed-lines, diamonds),* x=*128mm (double-dotted-dashed lines, upper-triangles),* x=*168mm (long-dashed-lines, circles). The wall is at* y = *3.5 mm and the symmetry plane at* y = *0. From Ref. [22].*

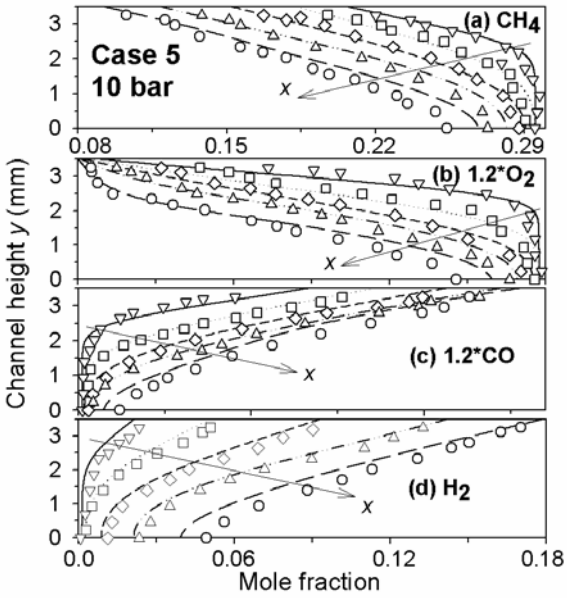

Figure 6: *Predicted (lines) and measured (symbols) profiles of species mole-fraction for Case 5 of Table 1. From Ref. [22].*

4.1.2. Homogeneous ignition

The onset of homogeneous ignition is a safety concern in CPO-based high-pressure systems (e.g. turbines). Comparisons between LIF-measured and predicted CH_2O distributions are illustrated in Fig. 7. Case 1 was specifically included so as to investigate homogeneous ignition at a much higher CO/H_2 ratio. The predicted levels of formaldehyde ranged from 1000 to 4100 ppmv. The onset of homogeneous ignition (x_{ig}), shown with the green arrows in Fig. 7, was defined in both measurements and predictions by the location where the formaldehyde levels rose to 5% of their maximum flame value. There was an overall good agreement between the measured and predicted x_{ig} (within 5% for Cases 1, 4 and 5 and within 20% for Cases 2 and 3).

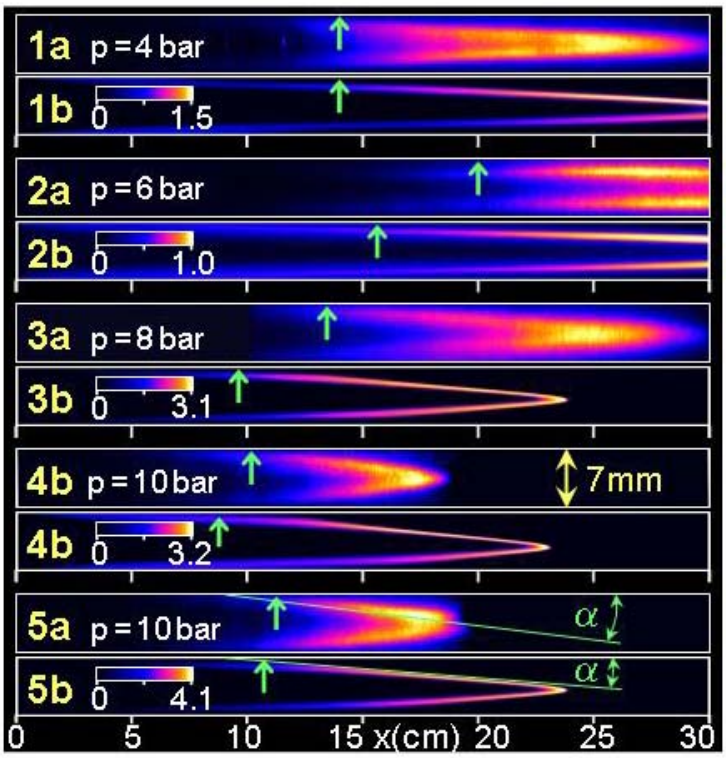

Figure 7: *(a) LIF-measured, and (b) numerically predicted distributions of formaldehyde (CH_2O) for the five cases of Table 1. The color bars provide the CH_2O in ppmv x 10^{-3}. Data from Ref. [22].*

4.2 Impact of H_2O and CO_2 dilution on steady catalytic partial oxidation

Steady experiments were carried out in the subscale gas turbine reactor of Fig. 3 with a 1%Rh/ZrO_2 catalyst. The experimental conditions are provided in Table 2. The pressure was 5 bar, the inlet temperatures (T_{IN}) ranged from 473 to 623 K and the inlet velocities increased with rising T_{IN} so as to maintain the same mass throughput. The gas hourly space velocity (GHSV) was in all cases $8x10^5$ hr^{-1} and the computed residence times in the catalytic section (accounting for the flow acceleration due to heating) ranged from 7 ms (Case 1) to 7.8 ms (Case 4). The equivalence ratio was $\varphi = 4$ and the dilution comprised 46.3% H_2O and 23.1% CO_2 per volume.

Case	p (bar)	U_{IN} (m/s)	T_{IN} (K)	Re_{IN}
1	5	5.1	623	590
2	5	4.7	573	637
3	5	4.3	523	689
4	5	3.9	473	755

Table 2: *Experimental conditions for steady honeycomb-reactor tests: pressure, inlet velocity, temperature, and Reynolds number. The inlet volumetric compositions for all cases are: 20.4% CH_4, 10.2% O_2, 46.3% H_2O and 23.1% CO_2.*

4.2.1 Comparisons between measurements and predictions

Comparisons between measured and predicted major species mole fractions and temperatures (the latter at x = 55 mm) are summarized in Table 3 for all cases of Table 2. The measured wet composition in Table 4 was assessed by carrying out balances for the C, H and O elements. The chemical scheme underpredicted somewhat the methane conversion and overpredicted the extent of the complete over the partial oxidation route; the latter was manifested by the lower predicted synthesis gas and higher complete oxidation products. The relative deviations between measured and predicted mole fractions increased with decreasing inlet temperature but were maintained within 20%. Nonetheless, the lower inlet temperature Cases 3 and 4 were marginally interesting for steady gas-turbine operation and, in particular, for approaches with large exhaust gas recycle.

Axial profiles of the predicted wall temperature (T_W), the average (over the radial distance r_h) gas temperature (T_{gas}), and the average methane and hydrogen mole fractions are depicted in Fig. 8 for Cases 1 and 4. The temperature comparisons in Fig. 8a were especially encouraging at x = 27 and 55 mm: the thermocouple measurements were bounded by T_W and T_{gas} (see also Table 3), suggesting that the numerical model realistically reproduced the temperature evolution along the reactor. On the other hand, the particularly good agreement between measured and predicted temperatures in the lower T_{IN} case (Fig. 3b) at x = 55 mm reflected to some extent the counteracting effects of lower predicted CH_4 conversion and higher selectivity to complete oxidation products.

Case	CH_4 (%)		O_2 (%)		H_2 (%)		CO (%)		H_2O (%)		CO_2 (%)		T (K)	
	Exp. Dry *Wet*	Sim. Dry *Wet*	Exp. Dry *Wet*	Sim. Dry *Wet*	Exp. Dry *Wet*	Sim. Dry *Wet*	Exp. Dry *Wet*	Sim. Dry *Wet*	Exp. Dry *Wet*	Sim. Dry *Wet*	Exp. Dry *Wet*	Sim. Dry *Wet*	Exp. T_D	Sim. T_W T_{gas}
1	12.8 *(7.4)*	13.1 *(7.4)*	0.3 *(0.1)*	1.5 *(0.8)*	33.3 *(19.3)*	31.3 *(17.7)*	14.3 *(8.3)*	13.8 *(7.8)*	- *(42.0)*	- *(43.5)*	39.4 *(22.8)*	40.4 *22.8*	1054	1062 *1054*
2	13.6 *(7.7)*	14.7 *(8.1)*	0.5 *(0.3)*	1.6 *(0.9)*	31.6 *(17.9)*	28.7 *(15.8)*	13.5 *(7.6)*	13.7 *(7.5)*	- *(43.2)*	- *(44.8)*	40.9 *(23.2)*	41.3 *22.8*	1041	1048 *1037*
3	14.8 *(8.3)*	16.4 *(8.8)*	0.9 *(0.5)*	1.7 *(0.9)*	29.6 *(16.5)*	26.1 *(14.3)*	12.5 *(7.0)*	13.4 *(7.2)*	- *(44.2)*	- *(46.0)*	42.2 *(23.6)*	42.4 *22.9*	1028	1035 *1019*
4	16.1 *(8.9)*	18.1 *(9.5)*	1.3 *(0.7)*	1.9 *(1.0)*	27.9 *(15.5)*	23.4 *(12.7)*	12.2 *(6.7)*	13.1 *(6.9)*	- *(44.6)*	- *(47.2)*	42.5 *(23.5)*	43.5 *23.0*	1020	1021 *1001*

Table 3: *Comparison between experiments and simulations for the conditions of Table 2: volumetric exit compositions (%, on dry and wet basis) and temperature at the end of the catalytically active section (position D in Fig. 3a, x = 55 mm). Results from Ref. [11].*

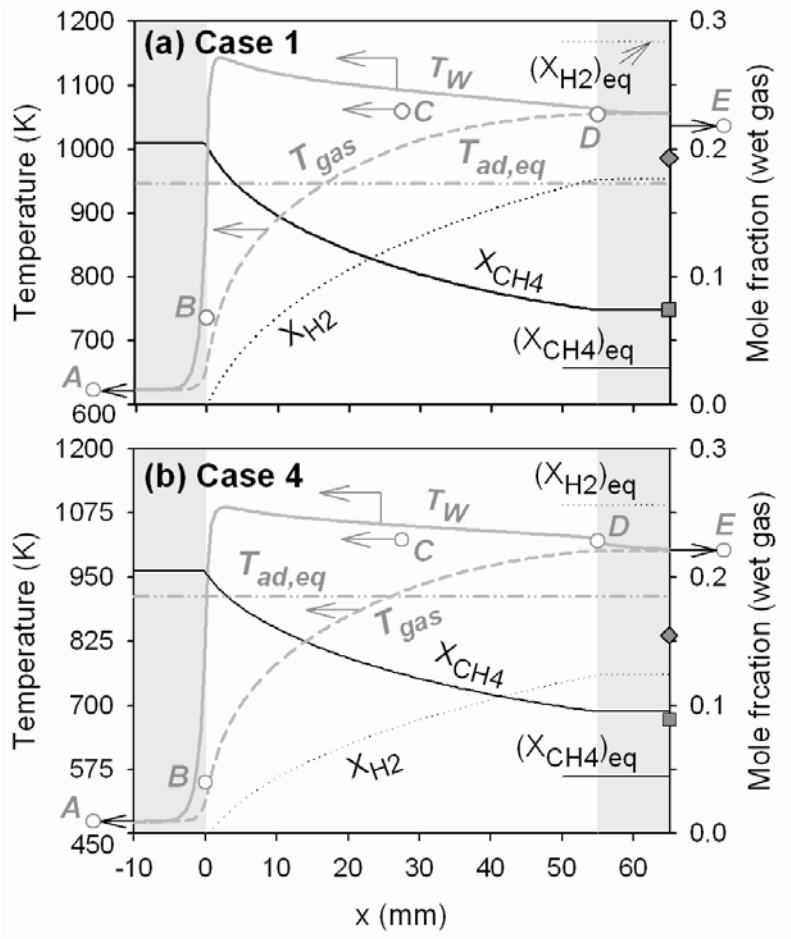

Figure 8: *(a) Axial profiles of temperature and species for: (a) Case 1 and (b) Case 4. Predictions: wall temperature T_W (solid gray lines), mean gas temperature T_{gas} (dashed gray lines), mean CH_4 mole fraction (solid lines), mean hydrogen mole fraction (dotted lines). Adiabatic equilibrium calculations are also provided for the gas temperature and the mole fractions of CH_4 and H_2 ($T_{ad,eq}$, $X_{CH4,eq}$ and $X_{H2,eq}$, respectively). Measurements: temperature (open circles), outlet H_2 mole fraction (filled diamond), outlet CH_4 mass fraction (filled square). The shaded areas denote the inactive reactor length. Results from Ref. [11].*

4.3 Transient light-off and extinction studies in methane CPO with large exhaust gas recycle

The experimental conditions are provided in Table 4. Cases 1 to 9 referred to CPO of CH_4/O_2 with 69.4% vol. EGR dilution (46.3% H_2O and 23.1% CO_2) and a CH_4 to O_2 equivalence ratio of four; in Case 10 the EGR dilution was 75% vol. and φ = 2.5. Cases 11 to 14 referred to CPO of $CH_4/O_2/N_2$ mixtures with an O_2 to N_2 molar ratio of 0.24. In Cases 1 to 9 the pressure was 5 bar and the mass throughput ($\rho_{IN}U_{IN}$) was maintained constant. The CPO tests without EGR (Cases 11 to 14) were carried out at 3 bar, again at a constant mass throughput. Laminar flows were established in all cases, with incoming Reynolds numbers less than 580 in each individual channel of the honeycomb. The computed residence times (accounting for flow acceleration due to heating) ranged from 8.8 to 11.9 ms. The gas hourly space velocity (ratio of the incoming volumetric flow rate, at standard conditions, to the volume of the coated reactor section) was 7.4×10^5 h^{-1} in Cases 1 to 9, 6.9×10^5 h^{-1} in Case 10 and 5.2×10^5 h^{-1} in Cases 11 to 14, which were realistically high for gas-turbine CPO systems.

Case	Type	φ	p (bar)	U_{IN} (m/s)	T_{IN} (K)	CH_4 (%)	O_2 (%)	H_2O (%)	CO_2 (%)	N_2 (%)	Catalyst Rh wt%	B [(b)]
1	Ign.	4.0	5	5.6	680	20.4	10.2	46.3	23.1	-	1.0	4.5
2	Ext.	4.0	5	5.1	623	20.4	10.2	46.3	23.1	-	1.0	4.5
3	Ext.	4.0	5	4.7	573	20.4	10.2	46.3	23.1	-	1.0	4.5
4	Ext.	4.0	5	4.3	523	20.4	10.2	46.3	23.1	-	1.0	4.5
5	Ext.	4.0	5	3.9	473	20.4	10.2	46.3	23.1	-	1.0	4.5
6	Ign.	4.0	5	6.0	730	20.4	10.2	46.3	23.1	-	0.5	3.0
7	Ext.	4.0	5	5.1	623	20.4	10.2	46.3	23.1	-	0.5	3.0
8	Ext.	4.0	5	4.3	523	20.4	10.2	46.3	23.1	-	0.5	3.0
9	Ext.	4.0	5	3.9	473	20.4	10.2	46.3	23.1	-	0.5	3.0
10	Ign.	2.5	5	5.5	725	13.9	11.1	50.0	25.0	-	1.0	4.5
11	Ext.	4.0	3	5.4	552	27.7	13.9	-	-	58.4	1.0	4.5
12	Ext.	4.0	3	4.5	470	27.7	13.9	-	-	58.4	1.0	4.5
13	Ext.	4.0	3	4.0	414	27.7	13.9	-	-	58.4	1.0	4.5
14	Ext.	4.0	3	2.9	298	27.7	13.9	-	-	58.4	1.0	4.5

Table 4: *Ignition and extinction tests in honeycomb reactor: test type (ignition, extinction-related), equivalence ratio, pressure, inlet conditions and volumetric composition, rhodium loading in catalyst, ratio of active-to-geometrical surface area. The ratio B (active to geometrical area) corresponds to a catalyst dispersion of 25.9 m^2/g-Rh for the 1% wt Rh loading and to 34.5 m^2/g-Rh for the 0.5% wt Rh loading. Conditions from Ref. [16].*

Light-off tests were carried out only for CPO with EGR, in Cases 1, 6 and 10. Therein, the inlet mixture compositions were first established in the reactor at inlet temperatures (T_{IN}) about 100 K lower than those of Table 4. The inlet temperatures were then ramped at a rate of +10 K/min so as to reach the value required to achieve catalytic ignition. Once light-off was achieved and steady operation was reached in Cases 1 and 6, extinction was subsequently investigated by reducing the inlet temperatures at a rate of 10 K/min. At certain inlet temperatures, steady states were established for periods as long as 15 min to accommodate gas-analysis measurements. Of those steady states, Cases 2 to 5 (pertaining to Case 1) and Cases 7 to 9 (pertaining to Case 6) will be presented herein. In the $CH_4/O_2/N_2$ extinction studies (Cases 11 to14), steady combustion was first established at the conditions of Case 1; the steam generator was then turned off, nitrogen was added, and the corresponding CH_4, O_2 and N_2 flows were adjusted to achieve the desired composition.

4.3.1 Catalytic ignition

Measured and predicted temporal profiles of temperature are provided in Fig. 9 for Case 1; predictions are shown for both the surface and the mean (radially-averaged) gas temperatures. Computed axial surface temperature profiles at selected time intervals are further given in Fig. 10. During the ramping of the inlet temperature in the experiments, a small catalytic reactivity was always present for T_{IN} > 600 K, which resulted in measured reactor temperatures slightly higher than the corresponding T_{IN}. For consistency with the experiments, the initial solid temperature in the numerical model (t = 0 in Figs. 9 and 10) has been obtained by solving first a transient case at a lower inlet temperature

(T_{IN} = 670 K) up to the time that yielded surface temperatures close to the measurements. It is, nonetheless, clarified that the small initial temperature excursions above T_{IN} = 680 K (less than 25 K at t = 0, as shown in Figs. 9 and 10) had a minimal impact on the subsequent time evolution of the ignition event.

The predictions reproduced well, at all four positions, the measured elapsed times for the onset of sharp temperature rise, the temporal extent of the main transient event, and also the final temperatures. At position *E*, the relevant predictions of Fig. 9 referred to the reactor exit (x = 65 mm); therein the channel walls were inert, leading to predicted mean gas temperatures higher than the corresponding surface temperatures during the period of sharp temperature rise. The measured temperatures at the late ignition stages ($t \geq 10$ s), where steady-state has been practically reached, were in good agreement with the predicted surface temperatures (Fig. 9). An exception was location *B*, with measurements in-between the predicted surface and mean gas temperatures. However, this can be attributed to the very steep spatial temperature gradients at position *B* (see Fig. 10): an effective repositioning of thermocouple *B* at x = -0.3 mm could readily account for those differences. It is further noted that computations with $T_{IN} \leq 670$ K did not yield light-off (in the sense of a vigorous burning solution) for an integration period of up to 20 s, which was roughly threefold longer than the experimentally measured time needed to reach the steady-state wall temperature at $x \approx 0$ (see Figs. 9 and 10). This outcome was in good agreement with the experimentally assessed inlet temperature for ignition (T_{IN} = 680 K).

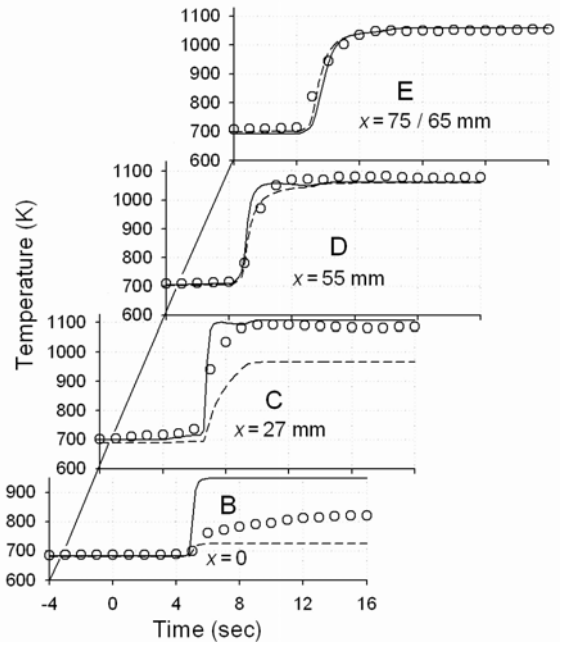

Figure 9: *Predicted (lines) and measured (symbols) temperatures at axial positions B through E for Case 1 (Table 4). Predictions are given for the wall temperature (solid lines) and the mean gas temperature (dashed lines). At position E, the measurements refer to the mean gas temperature 10 mm downstream of the reactor (x = 75 mm), while the predictions refer to the mean gas temperature at the reactor exit (x = 65 mm). Results from Ref. [16].*

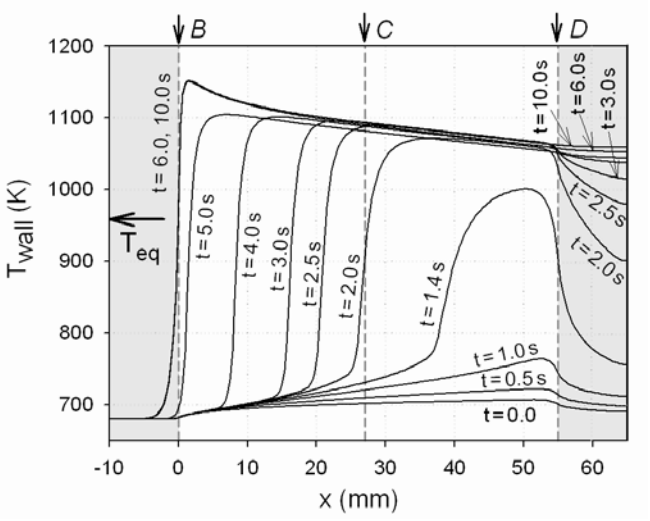

Figure 10: *Predicted axial profiles of wall temperature at different times for Case 1 (Table 4). The shaded areas denote the non-catalytic part of the reactor. The vertical arrows at B, C and D indicate the thermocouple locations inside the reactor. The horizontal arrow marked T_{eq} denotes the adiabatic equilibrium temperature. Results from Ref. [16].*

4.3.2 Catalytic extinction

Following catalytic ignition, vigorous burning states were established in Cases 1 and 6 of Table 4. Subsequently, the inlet temperature was ramped down so as to establish new steady states; at those steady states (typically every ΔT_{IN} = 50 K) detailed exhaust gas analysis was performed. Comparisons between predicted and measured exhaust gas compositions and temperatures for Cases 1 to 5 and Cases 6 to 9 are illustrated in Fig. 11. The accuracy in the measurements of Fig. 11 was particularly good: the C/H/O balances were better than 1% and the differences between inlet and outlet total enthalpies corresponded to an equivalent temperature differential of less than 15 K for all cases.

The lowest inlet temperature in the experiments was T_{IN} = 473 K, for both the 1% Rh (Fig. 11a) and the 0.5% Rh loading (Fig. 11b). At T_{IN} = 450 K steady vigorous combustion was also attained, however, water condensation at the colder solid walls of the mixing section prohibited any further reduction of the inlet temperature. For a steam partial pressure of 2.3 bar (Cases 1 through 9), thermodynamics indicated that water should start condensing at 400 K. Therefore, inlet temperatures below ca. 470 K were of no interest in practical CPO systems (e.g. gas turbines) with large EGR. Nonetheless, sustaining stable combustion at inlet temperatures as low as 470 K was of particular importance for part-load and idle turbine operation. Since water condensation prohibited the investigation of potential extinction at inlet temperatures below 473 K, additional experiments were carried out with $CH_4/O_2/N_2$ compositions without EGR (Cases 11 to 14); the O_2/N_2 molar ratio in those experiments was 0.24, close to that of air. The results of Fig. 12 indicated that stable and vigorous combustion could be sustained even at room temperature (T_{IN} = 298 K).

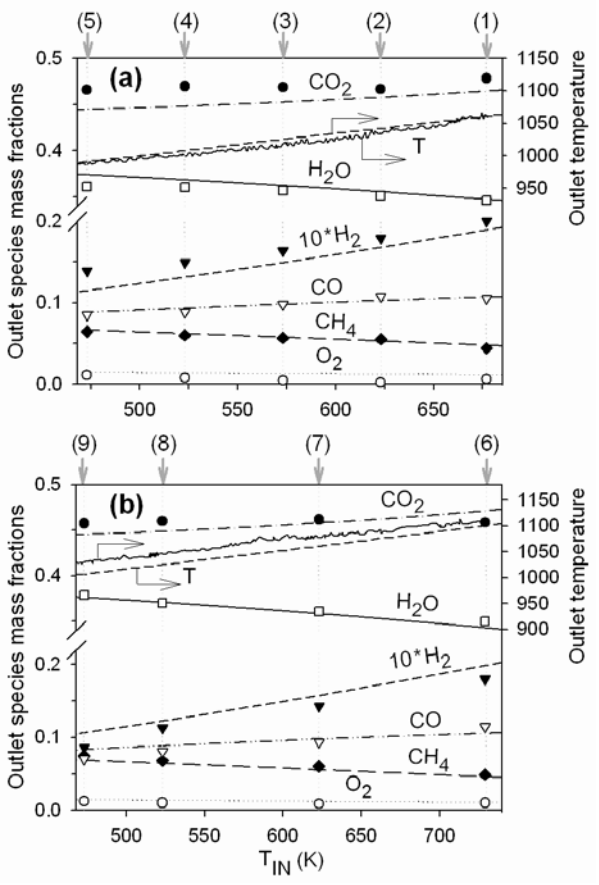

Figure 11: *Predicted (lines) and measured (symbols) outlet species mass fractions for: (a) Cases 1 to 5 and (b) Cases 6 to 9 of Table 4. The measured outlet temperature (solid line) at position E and the predicted outlet mean gas temperature (dashed line) are also shown. Results from [16].*

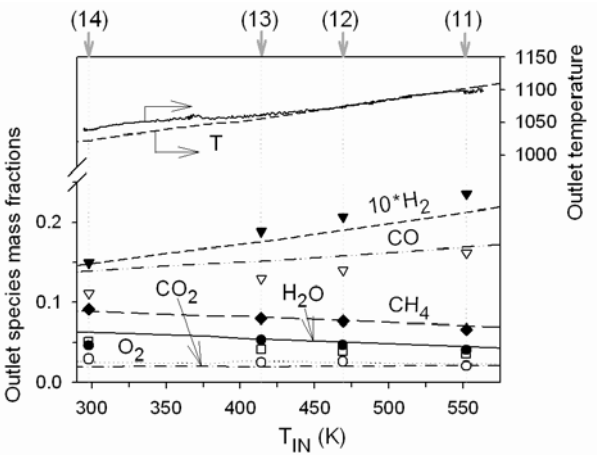

Figure 12: *Predicted (lines) and measured (symbols) outlet species mass fractions for Cases 11 to 14 of Table 4. The measured outlet temperature (solid line) at position E and the predicted outlet mean gas temperature (dashed line) are also shown. Results from [16].*

4.4 Effect of catalyst support in CPO of methane with large exhaust gas dilution

4.4.1 Catalyst characterization

The textural properties of the catalysts are presented in Table 5. Doping the ZrO_2 support with ceria resulted in an increase of the BET surface area from 21 to 44 m^2/g. The lowest surface area (6 m^2/g) was measured for the α-Al_2O_3 supported catalyst. The noble metal dispersion decreased in the following order: Rh/Ce-ZrO_2 > Rh/ZrO_2 > Rh/α-Al_2O_3. The factor *B* (ratio of active to geometrical surface area) was calculated based on H_2 chemisorption measurements and was subsequently used in Eqs. (9) and (10). The crystal structure of the support material for both fresh and tested samples of the Rh/Ce-ZrO_2 and Rh/ZrO_2 catalysts was determined by Raman microscopy. The spectra presented in Fig. 13 indicated that both monoclinic and tetragonal zirconia were present in the fresh Rh/ZrO_2 sample, whereas only tetragonal ZrO_2 could be detected for fresh Rh/Ce-ZrO_2. The peaks corresponding to different crystal structures are indicated by dashed lines. Testing under CPO conditions resulted in the formation of a pure monoclinic phase for the Rh/ZrO_2 catalyst. No phase transition occurred during reaction for the Rh/Ce-ZrO_2 sample, i.e. the tetragonal structure was maintained. The absence of phase transitions promoted high noble metal dispersion since encapsulation of Rh could be avoided. Stabilization of the tetragonal ZrO_2 phase by addition of small amounts of another dopant oxide, such as CeO_2 or Y_2O_3, has been reported previously [26, 27]. Furthermore, the enhanced surface area detected for the ceria-doped catalyst could be related to the stabilization of tetragonal ZrO_2.

Catalyst	BET surface area (m^2/g)	Active area (m^2 Rh/g Rh)	Rh dispersion (%)	B [(b)]
Rh/Ce-ZrO_2	44	43	11.8	10.0
Rh/ZrO_2	21	24	6.4	5.6
Rh/α-Al_2O_3	6	18	4.9	4.2

Table 5: *Textural properties of the employed catalysts. The BET surface area was measured on fresh powder samples whereas the active area refers to tested samples. B is the ratio of catalytically active to geometrical surface area. Data from [28].*

4.4.2 Measurements and predictions in the honeycomb reactor

To facilitate performance comparisons between different catalysts, the same experimental conditions were chosen for the three investigated supports (see Table 6). The pressure was 5 bar, the inlet temperatures (T_{IN}) were 623, 573 and 473 K, while the inlet velocities (U_{IN}) increased with rising T_{IN} so as to maintain the same reactor mass throughput. The flow was laminar with inlet Reynolds numbers (based on the channel hydraulic diameter) as high as 755 (see Table 6). In all cases the gas hourly space velocity (GHSV) was 7.4×10^5 h^{-1} and the computed residence times in the catalytic section of the reactor –accounting also for the flow acceleration due to heating– ranged from 7 ms (Cases 1, 4 and 7) to 7.8 ms (Cases 3, 6 and 9). The methane-to-oxygen equivalence ratio was $\varphi = 4.0$ and the dilution comprised 46.3% H_2O and 23.1% CO_2 per volume.

As seen in Fig. 13 and Table 7, the agreement between predictions and measurements is good. The simulations consistently somewhat underpredicted (overpredicted) the H_2 (H_2O) molar compositions. For the higher inlet temperatures T_{IN} = 623 and 573 K and for all catalyst supports, the relative differences between measured and predicted species compositions were less than 10%, except for the scarce O_2. In Cases 3, 6 and 9 with T_{IN} = 473 K, the discrepancies were as high as 15%. Moreover, the C/H/O element balances in the measurements of Table 7 were better than 1%.

For the same inlet conditions, the predictions indicated that an increase in Rh dispersion (Ce-ZrO_2 > ZrO_2> α-Al_2O_3) led to slightly higher methane conversion and lower surface temperatures (Fig. 6 and Table 4), higher H_2 and CO yields and selectivities and correspondingly higher H_2O consumption (Table 7). The measurements in Table 7 supported the aforementioned trends of the predictions. A slightly higher deviation between experiments and predictions was evident for the hydrogen

yields and methane conversions of the Ce-ZrO_2 support cases; however, those differences were mostly within the experimental uncertainty. It was thus evident that the key parameter controlling the methane conversion, synthesis gas yields and reactor temperature, at least in CPO with large EGR, was the noble metal dispersion.

Case	Catalyst support	p (bar)	T_{IN} (K)	U_{IN} (m/s)	Re_{IN}
1	Ce-ZrO_2	5	623	5.1	590
2	Ce-ZrO_2	5	573	4.7	637
3	Ce-ZrO_2	5	473	3.9	755
4	ZrO_2	5	623	5.1	590
5	ZrO_2	5	573	4.7	637
6	ZrO_2	5	473	3.9	755
7	α-Al_2O_3	5	623	5.1	590
8	α-Al_2O_3	5	573	4.7	637
9	α-Al_2O_3	5	473	3.9	755

Table 6: *Experimental conditions in the honeycomb reactor: pressure, inlet temperature, inlet velocity, and inlet Reynolds number. In all cases the inlet volumetric composition is 20.4% CH_4, 10.2% O_2, 46.3% H_2O, 23.1% CO_2, and the rhodium loading in the catalyst is 1 %wt.*

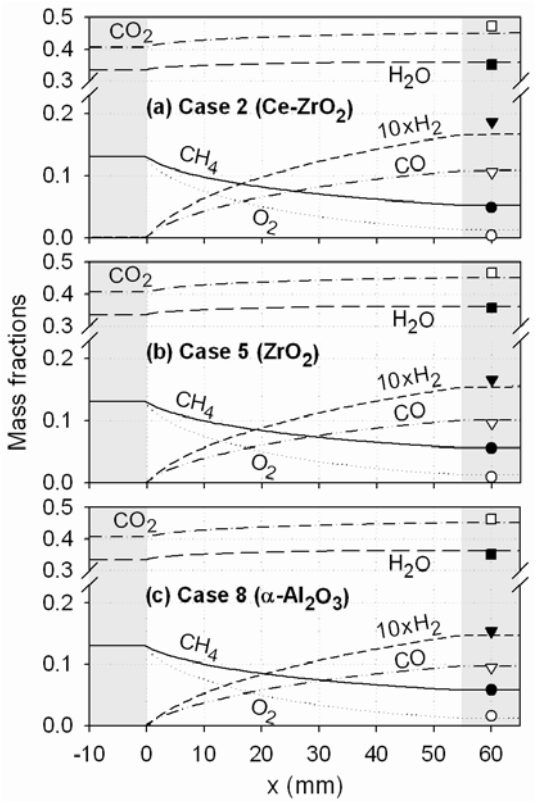

Figure 13: *Predicted axial profiles of average species mass fractions for Cases 2, 5 and 8 of Table 6. The measured exhaust gas composition is shown with symbols (open squares: CO_2, filled squares: H_2O, filled triangles: $10xH_2$, open triangles: CO, filled circles: CH_4, open circles: O_2). The shaded areas denote the inactive reactor length. Results from Ref. [28].*

Case	CH_4		O_2		H_2		CO		H_2O		CO_2		T *(K)*	
	Exp.	Sim.	Exp.	Sim.	Exp.	Sim.	Exp.	Sim.	Exp.	Sim.	Exp.	Sim.	Exp.	*Sim.*
1	6.0	6.4	0.1	0.8	21.0	19.9	8.8	8.6	41.4	42.0	22.7	22.3	1033	1009 1007
2	6.5	7.1	0.2	0.8	19.9	17.9	8.1	8.4	42.1	43.4	23.2	22.3	1022	995 992
3	7.4	8.6	0.2	1.0	16.8	14.3	8.2	7.7	44.2	46.0	23.2	22.4	978	966 961
4	6.8	6.9	0.5	0.8	19.4	18.7	8.3	8.2	42.1	42.8	22.9	22.6	1031	1033 1032
5	7.5	7.6	0.6	0.8	17.9	16.8	7.5	7.9	43.3	44.2	23.2	22.6	1027	1018 1015
6	8.8	9.3	0.6	1.0	14.9	12.7	6.8	7.1	45.1	47.1	23.8	22.8	994	998 994
7	7.5	7.2	0.9	0.8	18.9	18.1	7.8	8.0	42.1	43.3	22.8	22.7	1020	1046 1045
8	8.1	7.9	1.1	0.9	16.9	16.2	7.5	7.7	43.1	44.6	23.3	22.7	997	1030 1028
9	9.7	9.3	1.4	1.0	13.5	12.7	6.2	7.1	45.3	47.1	23.9	22.8	964	998 994

Table 7: *Comparison of measured and simulated volumetric exhaust composition (%) and temperature for the cases of Table 6. The temperature measurements refer to position E in Fig. 3(a), while in the simulations refer to x = 65 mm. In the simulations the upper value is the wall temperature and the lower value is the mean gas temperature. Results from Ref. [28].*

5. Diskussion

5.1 Validation of hetero-/homogeneous chemical reaction schemes.

5.1.1 Production of synthesis gas

The O_2 profiles in Figs. 5 and 6 indicated a mass-transport-limited catalytic conversion (manifested by the very low O_2 levels at the wall). In the upstream regions of minimal gas-phase pathway participation, there was always O_2 available (Figs. 5b, 6b). Figure 14 provides the computed streamwise profiles of the average (over the 7 mm channel height) species mole fractions and the thermocouple-measured upper and lower wall temperatures for Cases 2 and 5 of Table 1. Streamwise profiles of the computed catalytic and gas-phase species production rates (the latter integrated over the 7 mm channel-height) are provided in Fig. 15 for Cases 2 and 5. In the first ~3 cm of the reactor, the O_2/CH_4 catalytic destruction ratio ranged between one and two (Fig. 14), demonstrating a strong contribution of complete oxidation ($CH_4+2O_2 \rightarrow 2H_2O+CO_2$) in addition to CPO ($2CH_4+O_2 \rightarrow 4H_2+2CO$). Farther downstream, the destruction rate of CH_4 overtook that of O_2, and the molar ratio H_2/CO approached two at the end of the catalytically-dominant zones (Fig. 14a). The total oxidation at the upstream locations resulted in very steep transverse wall gradients of H_2O and CO_2 (see the first two profiles in Fig. 6(c, f)).

Water was catalytically produced at $x \leq 100$ mm (Fig. 15a) and $x \leq 92$ mm (Fig. 15b). Farther downstream, the catalyst turned to a sink of H_2O due to steam reforming ($CH_4+H_2O \rightarrow CO+3H_2$). Moreover, even well-downstream the onset of homogeneous ignition ($x > x_{ig}$), the catalytic pathway continued to play a pivotal role (Fig. 15); therein, the catalyst consumed CH_4 and H_2O, while it produced H_2, CO and CO_2. This was a result of heterogeneously-catalyzed steam reforming, which was responsible for H_2/CO molar ratios approaching three at the reactor exit (Fig. 14a). The catalytic production of CO_2 was due to the water gas shift reaction $CO+H_2O \rightarrow CO_2+H_2$. The pure catalytic methane conversion (before the onset of appreciable gas-phase contribution) was as high as 17%, with a hydrogen selectivity (based on the stoichiometry of the partial oxidation reaction) of up to 85%. For a given methane conversion, an increase in pressure from 4 to 10 bar decreased the hydrogen selectivity by a factor of ~1.50 to ~1.15. However, this effect reflected the lower surface temperatures of the higher-pressure cases (Fig. 14). Computations at a constant mass throughput and wall temperature (from 900 to 1100 K) have shown that an increase in pressure from 4 to 10 bar decreased only mildly the methane conversion and had practically no impact on the hydrogen selectivity. Those findings were in agreement with lower-pressure experiments (1.4 to 5.5. bar [26]) of CH_4/air CPO without dilution.

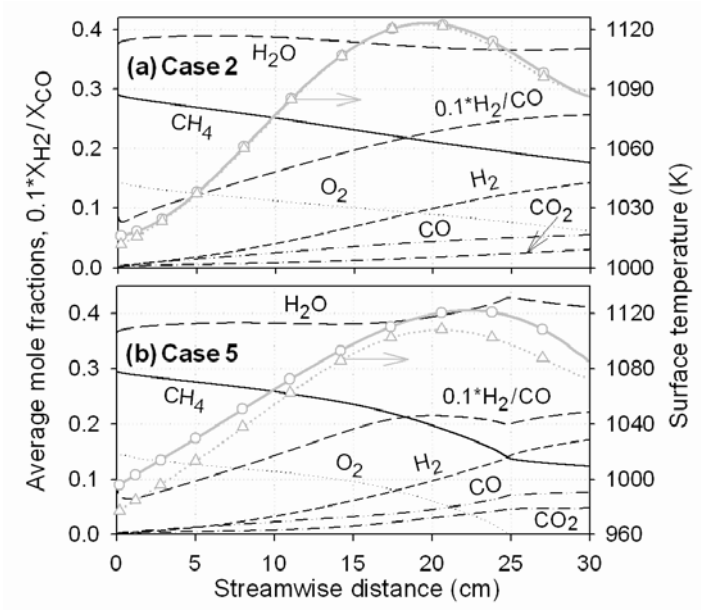

Figure 14: *Computed streamwise profiles of transverse-averaged species mole fractions. Streamwise profiles of wall temperatures (gray lines) fitted through the thermocouple measurements (circles: upper wall, triangles: lower wall). The sharp bends at x≈25 cm in (b) are associated with the end of the flame zone (Fig. 7(5b)). From Ref. [22].*

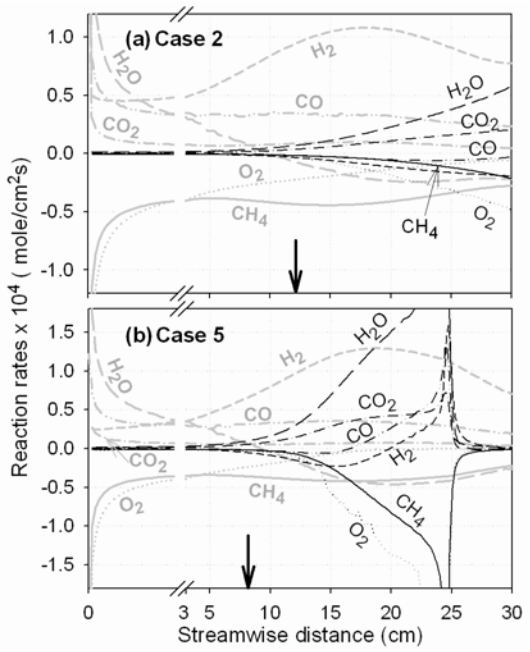

Figure 15: *Computed species production rates (gray lines: catalytic, black lines: gaseous). For clarity, the initial 3 cm are expanded. The thick arrows indicate the position where gas-phase contribution becomes appreciable. From Ref. [22].*

5.1.2 Gas-phase combustion

Despite the good homogenous ignition predictions (Fig. 7), there were differences in the spatial distribution of formaldehyde. The predicted formaldehyde was concentrated in thin reaction zones, whereas the measurements indicated a broader distribution in the pre-flame region. The latter was not an experimental artifact as evidenced by the following analysis. Tuning the excitation wavelength off-resonance revealed no significant background signal contribution. This was not surprising, since broadband fluorescing poly-aromatic-hydrocarbons (PAH) were only formed downstream the end of the flame at the reactor exhaust (as visibly seen and also as attested by LIF measurements in the exhaust at shallow optical collection angles). An elongation by a factor of two of the apparent formaldehyde zone has been reported in LIF measurements of non-preheated, atmospheric-pressure stoichiometric and slightly rich methane/air flames due to the exaggerated signal contribution of the colder (and hence higher density) zones upstream of the flame and due to quenching variations [29]. However, this effect is diminished in the present experiments due to mixture preheat, moderate flame temperatures (up to 1620 K at the channel center), and small changes of the gas composition (due to the substantially fuel-rich mixtures and the large H_2O dilution). Formaldehyde is known to form upstream of the flame front [29], however, it appears that the employed reaction scheme underestimates the contribution of those zones. Sensitivity analysis has further indicated that homogeneous ignition was affected by the H_2 and CO adsorption/desorption steps, as they determined the composition of the ignitable gaseous mixture. The small differences between Raman measurements and predictions could induce a ~3% difference in x_{ig}. This chemistry coupling has nevertheless exemplified the importance of the present combined hetero-/homogeneous investigations.

The measured flame sweep angles (denoted by α in Fig. 7(5)) were reproduced well by the predictions only at pressures up to 8 bar. In Cases 4 and 5 (10 bar), the measured flame lengths were noticeably shorter than the predicted ones, suggesting that the employed gas-phase scheme underpredicted the propagation characteristics (laminar flame speeds) at those mixture compositions and pressures. However, in practical CPO systems the main requirement on the gas-phase scheme is to capture igni-

tion delay (i.e. x_{ig}) and not propagation characteristics. Despite some apparent deficiencies of the employed reaction scheme, the present study has shown that it can reproduce the key safety issue of homogeneous ignition.

5.1.3 Conclusions of Section 5.1

The partial catalytic oxidation of $CH_4/O_2/H_2O/CO_2/N_2$ mixtures over Rh/ZrO_2 was investigated experimentally with in situ, 1-D Raman and CH_2O planar LIF measurements. Numerical simulations have shown that:

a) The employed homogeneous reaction scheme, despite deficiencies in the extent of the formaldehyde zone and its propagation characteristics at 10 bar, reproduced well the onset of homogeneous ignition.

b) The heterogeneous reaction scheme provided good agreement to the synthesis gas yields overpredicting slightly the partial over the total oxidation routes. The addition of H_2O increased the CH_4 conversion and H_2 yields and decreased the CO yields, due to a corresponding enhancement in the O(s) and OH(s) surface coverage.

c) An increase in pressure from 4 to 10 bar had a minor effect on the methane conversion and hydrogen selectivity, while the addition of CO_2 had a minimal chemical impact.

5.2 Impact of H_2O and CO_2 dilution on steady catalytic partial oxidation

5.2.1 Synthesis gas production

The controlling chemical reactions are summarized below:

$CH_4 + 2O_2 = CO_2 + 2H_2O$	(complete oxidation)	(R1)
$2CH_4 + O_2 = 2CO + 4H_2$	(partial oxidation)	(R2)
$CH_4 + H_2O = CO + 3H_2$	(steam reforming)	(R3)
$CO + H_2O = CO_2 + H_2$	(water gas shift)	(R4)
$CH_4+CO_2 = 2CO + 2H_2$	(CO_2 reforming)	(R5)

The processes along the honeycomb channel are described using the simulations of Case 1 (Table 2). Computed 2-D distributions of the temperature and major species mole fractions are presented in Fig. 16. The underlying physicochemical processes are investigated with the aid of Figures 16, 17 (axial profiles of species molar catalytic production/destruction rates and selected rate-ratios) and 18 (axial profiles of radially-averaged species mass fractions). Mass rather than mole fractions were used in Fig. 18, so as to appropriately describe the species spatial evolution in the presence of non-equimolar reactions (R2, R3 and R5). This resulted in exit H_2O mole fractions lower than those of the inlet (Fig. 16f) despite the increase in water mass throughput (Fig. 18).

The peak in the H_2O and CO_2 mole fractions (Fig. 16f,g) at $x \approx 0$ and the accompanying peaks in the production rates of those species (Fig. 17a) were indicative of complete oxidation (R1) at the beginning of the catalyst. This reaction became mass-transport-limited already at $x \approx 0$ (manifested in Fig. 5c by the nearly zero levels of the deficient O_2 reactant at $r = 0.6$ mm). The CH_4/O_2 destruction ratio was 0.78 at $x = 0$ (Fig. 17b), demonstrating a non-negligible partial oxidation (R2) contribution. Partial oxidation products were readily formed at $x \approx 0$ (Fig. 16d,e). Over the length $2 \text{ mm} < x < 25$ mm, the H_2/CO production ratio was ~2.2, the CH_4/O_2 destruction ratio was ~1.2 and the H_2/CH_4 destruction/production absolute ratio was ~1.6 (Fig. 17b), pointing to the significance of both R1 and R2; in this zone oxygen was still available in the gas (Fig. 18) to accommodate the oxidation reactions. At $x > 39$ mm, where O_2 was largely depleted (Figs. 18 and 16c), there was a shift from production to destruction of H_2O (Fig. 17a). Steam reforming (R3) was considerable at those downstream parts, as also manifested by the increase of the H_2/CO production ratio to nearly three at the end of the catalyst. The continuous drop of the wall temperature along the reactor (Figs. 16a and 8a) concurred to the importance of this endothermic step. Water gas shift (R4) was also present at $x > 39$ mm and contributed to further enhancing the H_2/CO and H_2/CH_4 ratios (Fig. 17b). On the other

hand, CO_2 reforming (R5) had no contribution to the synthesis gas production. This is attributed to the fact that in the presence of $H_2O/O_2/CO_2$, H_2O or O_2 reforming reactions of methane are appreciably faster than CO_2 reforming.

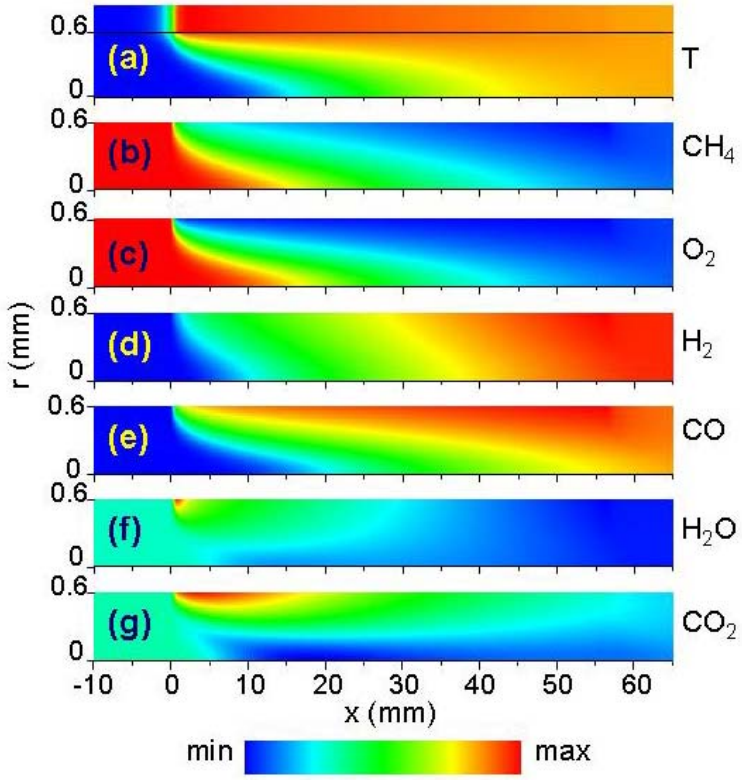

Figure 16: *Computed 2-D distributions of the temperature and species mole fractions for Case 1 of Table 2. The minimum and maximum levels of the color bar are: (a) T: 623 K to 1123 K, (b) CH_4: 0.061 to 0.204, c) O_2: 0.001 to 0.103, d) H_2: 0.0 to 0.184, e) CO: 0.0 to 0.090, f) H_2O: 0.432 to 0.528 and g) CO_2: 0.219 to 0.260. The centerline is located at r = 0 and the gas-solid interface at r = 0.6 mm; the catalytically active section spans the range $0 \le x \le 55$ mm. The temperature inside the solid (0.6 mm < r < 0.637 mm) is also shown in (a) on an expanded radial scale. From Ref. [11].*

The predicted methane conversion was 58.6%, a value acceptable for "catalytic rich combustion" with a post-catalyst flame zone. The water mass throughput increased along the reactor ($Y_{H2O,IN}$ = 0.332 and $Y_{H2O,OUT}$ = 0.357, see Fig. 18) despite the contribution of steam reforming and water gas shift reactions farther downstream. There was simply insufficient residence time at the given temperatures for the slow endothermic steam reforming to further increase the consumption of water and methane. The predicted wet gas outlet H_2 and CO mole (mass) fractions in Case 1 were 0.177 (0.016) and 0.078 (0.099), respectively. The partial oxidation product selectivities, weredefined as:

$$S_{H2} = \frac{0.5\, Y_{H2} / W_{H2}}{(Y_{CH4,IN} - Y_{CH4,OUT}) / W_{CH4}} \quad \text{and} \quad S_{CO} = \frac{Y_{CO} / W_{CO}}{(Y_{CH4,IN} - Y_{CH4,OUT}) / W_{CH4}}. \qquad (14)$$

For Case 1, S_{H2} = 0.84 and S_{CO} = 0.74. The definition of Eq. (14) is based on hydrogen produced from methane and it is maintained herein, despite the added H_2 production from H_2O.

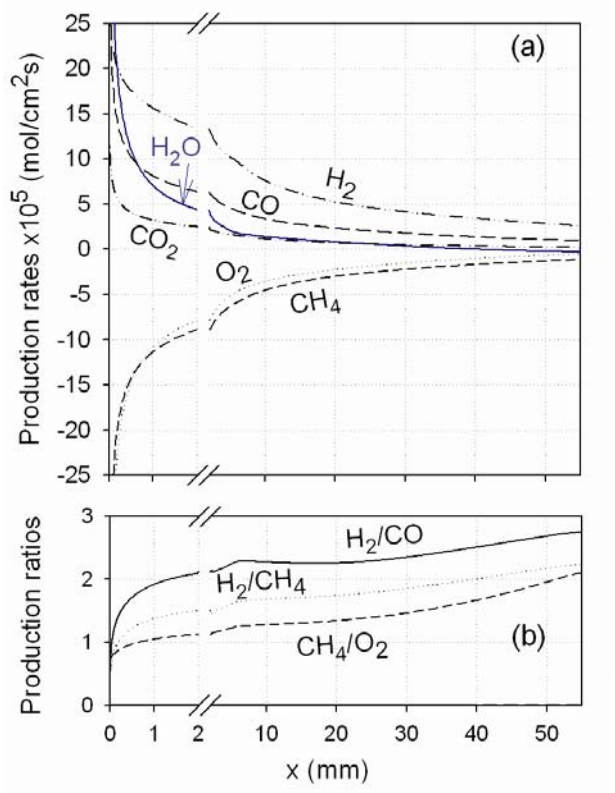

Figure 17: *Computed axial profiles (Case 1) of Table 2: (a) molar species catalytic production (or destruction) rates, and (b) rate-ratios for selected pairs of species (in H_2/CH_4, the absolute value is given). For clarity, the first 2 mm are expanded. Results from Ref. [11].*

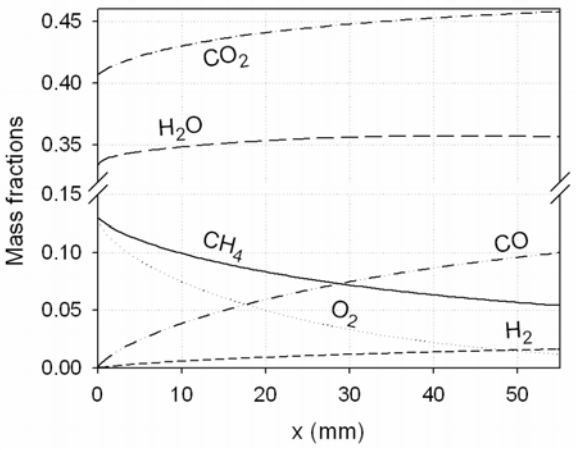

Figure 18: *Computed axial profiles of radially-averaged species mass fractions for Case 1 of Table 2. Results from Ref. [11].*

5.2.2 Impact of H_2O and CO_2 on synthesis gas production

To identify the impact of water on the synthesis gas yields and product selectivities, additional predictions have been carried out with the diluent H_2O replaced by a fictitious species H_2O^* that had the same thermodynamic and transport properties as H_2O but did not participate in any reaction. H_2O^* simulated only the incoming diluent whereas the catalytic pathway was still allowed to create combustion-generated H_2O. The wall temperature profile of Fig. 8a was imposed as energy boundary condition in the computations with H_2O^* so as to isolate the chemical effects of dilution. The surface coverage for Case 1 (H_2O dilution) and for the corresponding case with H_2O^* dilution is shown in Fig. 19. The axial profiles of radially-averaged major species mass fractions are presented in Fig. 20 for the H_2O^* dilution.

The presence of steam in the feed augmented the $H_2O(s)$ coverage by almost an order of magnitude (Fig. 19) due to the near equilibration of the H_2O adsorption/desorption reactions. The increase in $H_2O(s)$ also enhanced the O(s) coverage especially at the downstream locations were O_2 was largely depleted. The comparisons of Fig. 19 revealed a factor of six increase of O(s) for the H_2O-diluted case at x = 55 mm. The elevated O(s), led to enhanced methane depletion (Fig. 20). The reduced impact of the H(s)-consuming net reactions (H(s) + O(s) → OH(s) + Rh(s)) due to the increased OH(s)/O(s) ratio of the H_2O- compared to the H_2O^*-dilution resulted in a ~25% rise of H(s) for the former case (Fig. 19) that, in turn, promoted the H_2-producing desorption reaction. When H_2O was replaced by H_2O^* the comparisons in Fig. 20 revealed a decrease in both methane conversion (from 58.6% to 54.1%) and hydrogen exit mass fractions (from 0.016 to 0.012).

The addition of steam caused a significant drop in C(s) (Fig. 19) since the higher O(s) coverage accelerated the C(s)-depleting reaction C(s) + O(s) → CO(s) + Rh(s). The higher amounts of O(s) also favored the complete oxidation CO(s)+O(s) → CO_2(s)+Rh(s) against the CO desorption, thus reducing

the yields of CO and increasing those of CO_2 (Fig. 20). When H_2O was replaced by H_2O*, the CO exit mass fractions increased from 0.099 to 0.109. The selectivities for the H_2O*-dilution, computed from Eqs. (14), were S_{H2} = 0.67 and S_{CO} = 0.87. Therefore, the presence of 46.3% H_2O increased the H_2 selectivity by 25% and reduced the CO selectivity by 15%. Within the context of gas-turbine "catalytic rich combustion", the increase in hydrogen selectivity is particularly beneficial for the stabilization of the post-catalyst flame.

The impact of CO_2 dilution was investigated in a similar fashion by introducing a fictitious species CO_2*. The computations revealed that neither the CH_4 conversion nor the H_2 and CO selectivities were affected by this change. When CO_2 was replaced by CO_2*, the only noticeable change was a drop in the CO_2(s) coverage by up to a factor of two; nonetheless, the CO_2(s) coverage was too low (Fig. 19) to meaningfully affect the other surface species. This difference is attributed to the fact that in the presence of $H_2O/O_2/CO_2$, H_2O or O_2 reforming reactions of methane are appreciably faster than CO_2 reforming [30].

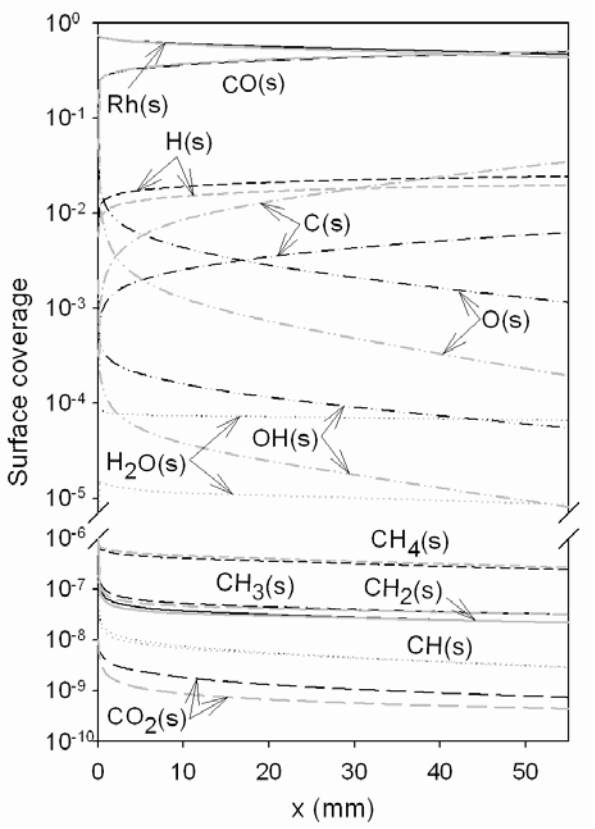

Figure 19: *Surface coverage for Case 1 (black lines) and for the same case when the inlet 46.3% H_2O replaced by equal amount of chemically inert H_2O* (gray lines). From Ref. [11].*

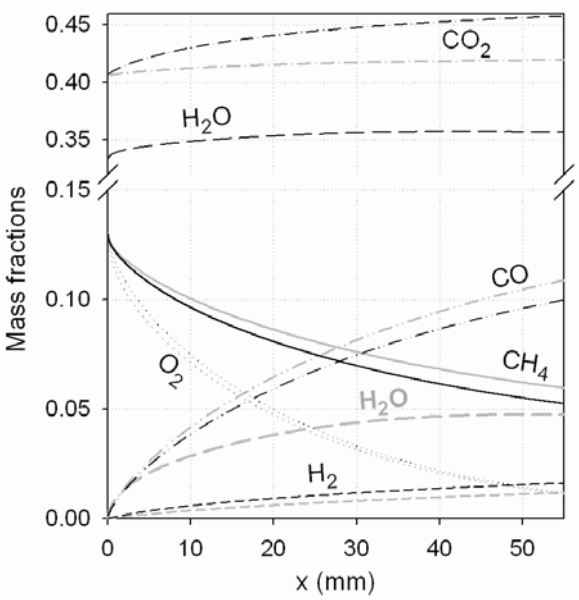

Figure 20: *Computed axial profiles of radially-averaged species mass fractions for Case 1 (black lines) and corresponding profiles when the inlet water content of Case 1 is replaced by equal amount of chemically inert H_2O* (gray lines). From Ref. [11].*

5.2.3 Conclusions of Section 5.2

a) The employed catalytic reaction scheme reproduced the measured temperatures along the reactor as well as the measured exit composition, overpredicting mildly the impact of the total over the partial oxidation route. The overprediction was more pronounced at lower inlet temperatures.

b) The reactor thermal management was an important issue in practical reactors. The surface temperatures exceeded by as much as 200 K the adiabatic equilibrium temperature due to the short residence times and the multiple reaction pathways that included complete and total oxidation, steam reforming and water gas shift. It was shown that thermal management approaches solely based on heat transfer mechanisms in the solid substrate were inadequate in controlling the surface temperatures.

c) The presence of H_2O provided a source for surface oxygen and hydroxyl-radicals, O(s) and OH(s), which in turn resulted in higher methane conversion, higher H_2 and lower CO selectivity. This was highly desirable for CPO-based turbine reactors as hydrogen can aid the stabilization of the post-catalyst gaseous combustion zone. The higher hydrogen selectivities were attributed to the more favorable competition of hydrogen desorption ($2H(s) \rightarrow 2Rh(s)+H_2$) over surface oxidation ($H(s)+O(s) \rightarrow Rh(s)+OH(s)$ and $H(s)+OH(s) \rightarrow Rh(s)+H_2O(s)$). On the other hand, the CO selectivity decreased due to the promotion of its surface oxidation ($CO(s)+O(s) \rightarrow Rh(s)+CO_2(s)$).

d) The addition of CO_2 had a minor impact on the CH_4 conversion and the H_2 or CO selectivity during CPO with large H_2O dilution. Therefore, CO_2 reforming is not important in short contact time gas-turbine reactors with exhaust recirculation.

5.3 Transient light-off and extinction studies in methane CPO with large exhaust gas recycle

The underlying chemical processes during light-off are discussed with the aid of Figs. 21 and 22 that provide, at three selected times, the 2-D maps of temperature and major species mass fractions, and the species net production rates and selected production rate ratios, respectively. Ignition was initiated at the rear of the channel as shown in Figs. 10 and 21. Total oxidation of methane dominated at early times as manifested by the sharp rise of H_2O, CO_2 and temperature in Fig. 21a and by the ~0.5 value of the CH_4:O_2 molar consumption ratio at the far upstream location of the reaction zone (see Fig. 22a, $x \approx 36$ mm). H_2 and CO were not produced for $t < 1$ s, whereas at later times CO production commenced before that of H_2. At $t = 1.4$ s, both partial oxidation products were produced (Fig. 22a), giving rise to the observed very low levels of H_2 and CO in Fig. 21a. Following ignition, the reaction zone propagated upstream (Fig. 10) with an accompanying increase in peak surface temperature due to the gradual heat-up of the wall and the diminishing accumulation of heat in the solid mass. The peak temperature reached the front of the catalytically coated section at $t \approx 6$ s, while at $t \approx 10$ s steady-state had been practically achieved over the entire reactor length (Fig. 10). The wall and mean gas temperatures exceeded by as much as ~200 K the adiabatic equilibrium temperature ($T_{eq} = 959$ K, see Figs. 9 and 10), a condition typical in CPO reactors with residence times of a few milliseconds [11, 31].

5.3.1 Impact of H_2O and CO_2 dilution on catalytic ignition

Despite the added large amount of CO_2, the contribution of dry (CO_2) reforming was negligible as also shown in the previous steady-state investigation of Section 5.2 (see also Ref. [11]). The reason was that oxy- and H_2O-reforming reactions were considerably faster than dry reforming [32] and the dominance of the former steps was further accentuated by the present short contact times. The absence of dry reforming has also been attested in CH_4/air CPO without EGR [31, 33]. To investigate the impact of water on the synthesis gas yields and selectivities, additional predictions have been carried out for Case 1 (Table 4), whereby the 46.3% H_2O feed content was replaced by a fictitious species H_2O^* that had the same thermodynamic and transport properties as H_2O but did not participate in any reaction. H_2O^* simulated only the incoming steam whereas the catalytic pathway was still allowed to create combustion-generated H_2O. It was evident that the presence of water increased (decreased) the H_2 (CO) selectivity and slightly increased the methane conversion, while it moderated somewhat the surface temperatures. The reason was the same as elaborated in the previous steady-state CPO studies of Section 5.2. It was also shown that the added amount of H_2O facilitated steam reforming mainly

by depleting faster the water produced by total oxidation (R1) rather than by consuming the incoming steam itself (at any time, $Y_{H2O,OUT}(t) > Y_{H2O,IN}$). This was because the surface temperatures were moderate and the residence times too short for the slow endothermic steam reforming to dominate. Of importance in the present transient analysis, was that the chemical impact of water was already evidenced at early times (e.g. $t > 1.5$ s). However, the effect of added water grew to larger importance at later times when a significant extent of the channel attained high temperatures.

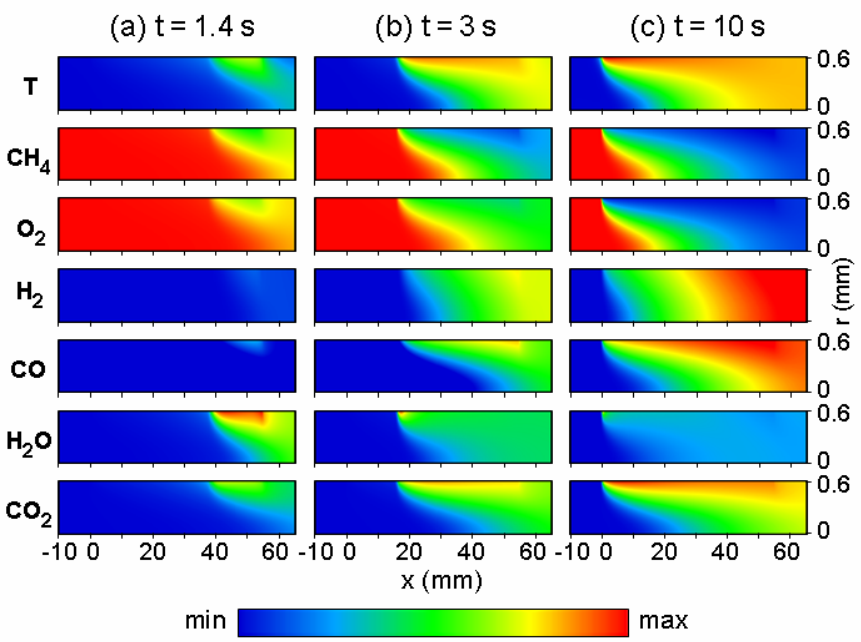

Figure 21: *Predicted 2-D distributions of temperature and species mass fractions for Case 1 at three times: (a) 1.4 s, (b) 3.0 s, and (c) 10.0 s. The maximum and minimum levels of the color bar are: T: 681 K to 1146 K, CH_4: 0.039 to 0.131, O_2: 0.0 to 0.131, H_2: 0.0 to 0.0186, CO: 0.0 to 0.123, H_2O: 0.332 to 0.398, and CO_2: 0.406 to 0.478. The centerline is at r = 0 and the gas-solid interface at r = 0.6 mm. The catalytically active part of the reactor extents over $0 \leq x \leq 55$ mm. Data from Ref. [16].*

Despite the chemical impact of H_2O and the associated somewhat lower surface temperatures (by as much as 26 K compared to the H_2O* dilution) due to the enhanced impact of steam reforming, the times required for the onset of ignition and for the propagation of the reaction zone to the front of the catalytic section ($x = 0$) were practically the same in both H_2O and H_2O* dilution. To isolate reactor parameters (heat conduction in the solid, etc.) from chemical effects, ignition delay times have been computed in a batch reactor, with only surface reactions included) using surface-to-volume ratio S/V = 33.3 cm^{-1}, so as to mimic the confinement of the channel experiments. The catalytic ignition delay times, τ_{ig}, (defined as the times required to reach the 50% rise between inlet and final temperatures) were practically independent of dilution type (15.2 ms for the H_2O and 15.0 ms for the H_2O*). The reason was that the dominant reaction controlling catalytic ignition (in either H_2O or H_2O* dilution) was the surface oxidation of CO(s) to CO_2(s). Upon ignition, CO(s) and free sites (Rh(s)) comprised the main surface coverage. During the ignition process, the rising CO(s) coverage reduced the amount of available free sites and hence inhibited ignition. It is nonetheless, instructive to consider not only the chemical but also the thermal impact of the aforementioned reaction. This reaction eventually led to the formation of CO_2, the oxidation CO $\rightarrow$ CO_2 being a main exothermic heat release step. The oxidation of H_2 to H_2O was less important, since the CO:H_2 molar ratio over the entire induction zone was at least ten. Catalytic ignition delay times were, therefore, dominated by total oxidation reactions forming CO_2, and as such they were not critically affected by reactions forming partial oxidation products. In summary, the chemical impact of H_2O dilution, although important during the time evolution of the light-off event, was minimal on the ignition delay times themselves.

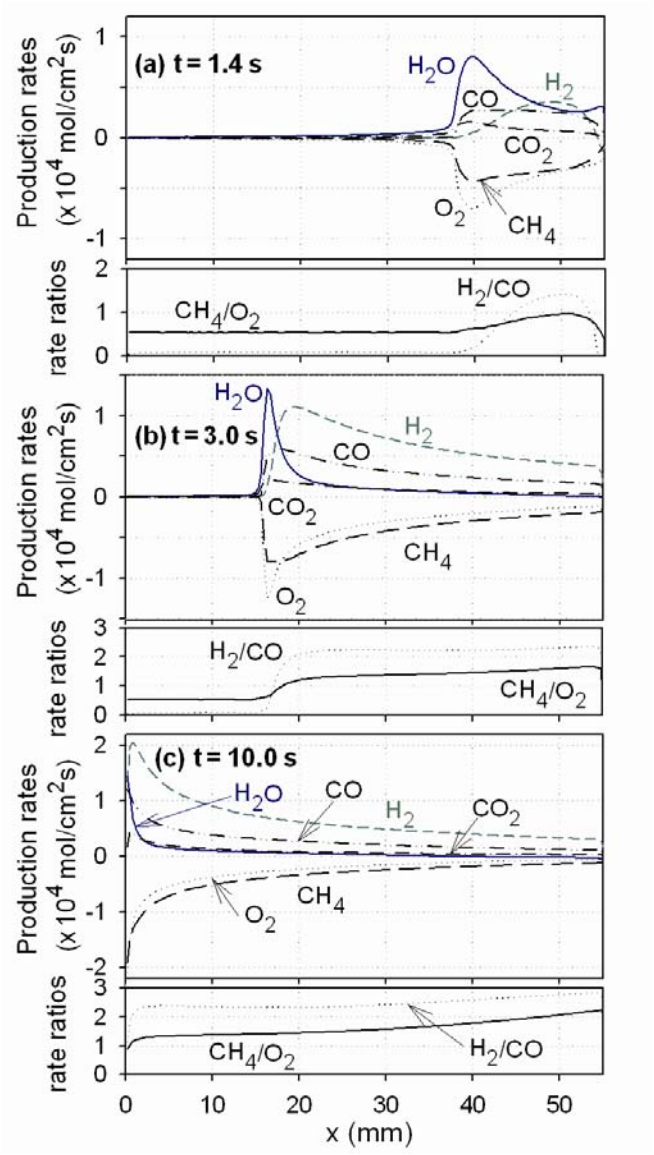

Figure 22: *Computed axial profiles (Case 1) of species molar production rates (solid lines: H_2O, short dashed lines: H_2, double-dotted-dashed lines: CO, dotted-dashed lines: CO_2, long dashed lines: CH_4, dotted lines: O_2) and production rate-ratios (solid lines: CH_4:O_2, dotted lines: H_2/CO) at three times: (a) 1.4 s, (b) 3.0 s, and (c) 10.0 s. From Ref. [16].*

5.3.2 Catalytic extinction

The resilience of CPO against extinction is explained below. When the inlet temperature decreased, there was a shift from partial to total oxidation regarding the H_2/H_2O species; this was manifested by the drop (rise) of the H_2 (H_2O) mass fraction in both experiments and predictions (Fig. 11). The predicted H_2 selectivity (Eq. (14)) decreased substantially from 0.91 at T_{IN} = 680 K to 0.70 at T_{IN} = 473 K. The CO and CO_2 mass fractions both decreased with decreasing inlet temperature, with the CO selectivity increasing slightly from 0.74 at T_{IN} = 680 K to 0.77 at T_{IN} = 473 K. Overall, the presence of total oxidation products was more pronounced at lower temperatures (the reason being that reforming reactions were thermodynamically favored at higher temperatures). The increased importance of the total oxidation pathway with decreasing T_{IN} led, in turn, to higher reactor exothermicity that compensated −to a great extent− for the drop in inlet temperature. For example, the difference in exhaust gas temperatures at T_{IN} = 473 and 680 K (Cases 1 and 5 in Fig. 11(a)) was only 70 K. Alternately, the computed heat release in Case 1 amounted to 45% of the heat release calculated when considering complete oxidation of methane; the corresponding number for Case 5 was 57%. It is further noted that the agreement between measurements and predictions in Fig. 11 was quite good; the predicted and measured species mass fractions were within 8% (the scarce O_2 was an exception) at $T_{IN} \geq 573$ and

within 15% at $T_{IN} \leq 523$. The predicted outlet temperatures were within 12 K (Fig. 11(a)) and 25 K (Fig. 11(b)) of the measurements. At lower inlet temperatures, the model appeared to slightly overpredict (underpredict) the route to CO (CO_2).

5.3.3 Key conclusions of Section 5.3

a) The employed heterogeneous reaction scheme reproduced the measured minimum inlet temperatures required for light-off, the elapsed times for the propagation of the reaction front, and the steady-state exhaust gas compositions in CPO with EGR at a fuel-to-oxygen equivalence ratio $\varphi = 4.0$. At $\varphi = 2.5$, however, only qualitative agreement was obtained and the numerical model overpredicted the synthesis gas yields.

b) The chemical impact of the added H_2O in the feed was already evident at the early stages of the transient catalytic ignition event and its importance further increased as steady state was approached. At steady state, the large H_2O dilution resulted in increased hydrogen selectivity, decreased CO selectivity and slightly increased methane conversion. The chemical impact of CO_2 dilution was minimal on both the transient event and the subsequent steady combustion.

c) Despite the significant chemical impact of H_2O dilution during the light-off process, the ignition delay times themselves were practically unaffected by its presence. The reason was that light-off times were dominated by total oxidation reactions and not by partial oxidation or reforming reactions leading to synthesis gas products. The key reaction affecting catalytic ignition was the surface oxidation of CO to CO_2, which was the main exothermic heat release step in the induction zone. The surface oxidation of H_2 to H_2O, on the other hand, was less significant due to the low amounts of H_2 formed in the induction zone.

d) Measurements and predictions indicated that vigorous combustion could be sustained at inlet temperatures as low as 473 K in CPO with EGR. In CPO without EGR, vigorous combustion was still possible with inlet temperatures as low as 298 K. The reason for the extended stability limits of CPO combustion was the shift from partial to total oxidation products –and hence to higher exothermicity– with decreasing inlet temperature.

e) Computed extinction characteristics obtained at various reactor residence times indicated that extinction in CPO with EGR was possible only at very short times (< 4 ms), which were not relevant to new power generation cycles. On the other hand, in CPO without EGR stable combustion was attained at residence times as short as 1 ms. The key parameter controlling catalytic extinction in CPO was the CO(s) coverage. Near extinction CO(s) increased, reducing the free sites and thus leading to catalyst poisoning.

f) The advantage of reactor materials with high thermal conductivity has been demonstrated for practical CPO systems. Moreover, operation at non-optimal stoichiometries ($\varphi = 2.5$) was shown to be beneficial in CPO with large EGR, due to the moderating effects of dilution on the maximum reactor temperature.

5.4 Effect of catalyst support in CPO of methane with large exhaust gas dilution

The reasons for the validity of the employed heterogeneous reaction scheme in Rh catalysts with different supports are elaborated below. Methane activation is generally considered to occur on the metal sites (Rh, Ni, Pt etc.) of supported catalysts for partial oxidation of methane, steam reforming, and carbon dioxide reforming (dry reforming) [34-37]. The main function of the support is to disperse the noble metal particles and prevent sintering. However, CeO_2 is also known for its oxygen storage capacity and ability to stabilize the support. Studies have shown that the oxygen transport properties of CeO_2 make it suitable for direct oxidation of methane to synthesis gas in the absence of gaseous oxygen [38]. This process occurs in two steps, first methane reacts with CeO_2, producing H_2 and CO. In the second step, ceria is re-oxidized by CO_2 or water. The activation of methane on CeO_2 is, however, insignificant in the presence of a noble metal. Pulse studies [39] have shown that methane decomposition occurs on the noble metal sites for $Rh/CeO_2/\gamma\text{-}Al_2O_3$. Therefore, any interaction of CH_4 with the support is most likely negligible for the catalysts in the present study.

Different reaction mechanisms for the reforming of methane over supported catalysts have been proposed. In steam reforming over a $Ni/MgAl_2O_4$ catalyst, [40] presented a reaction mechanism where both CH_4 and H_2O adsorbed dissociatively on surface Ni atoms. Other researchers proposed a Mars-van Krevelen type mechanism where the support played an active role [41, 42]. Methane was activated on the metal sites producing H_2 and carbon, whereas the co-reactant (CO_2 or H_2O) dissociated on reduced support sites. The adsorbed oxygen species then reacted with the carbon deposits at the support-metal interface.

The reaction mechanism involving active support sites has especially been reported for ceria-based catalysts [43-45]. The high oxygen transport capacity of ceria, which is related to the ability of ceria to shift between Ce^{3+} and Ce^{4+}, facilitates oxygen transport from the support to the metal sites. Studies have shown that the activity and stability of Ni/Al_2O_3 catalysts for dry reforming could be improved by adding CeO_2 [43]. Those improvements were attributed to the redox properties of ceria, resulting in continuous removal of carbonaceous deposits by reaction with lattice oxygen forming CeO_{2-x}. The reduced ceria was then re-oxidized by CO_2. When studying steam reforming, $Ni/Ce\text{-}ZrO_2$ catalysts were found to be more stable than Ni/Al_2O_3 [44]. However, no increase in activity was evident for this reaction when changing support to $Ce\text{-}ZrO_2$. Similar results, showing improved stability, have been reported for partial oxidation of methane over $Pt/Ce_xZr_{1-x}O_2$ catalysts [46].

In general, the addition of ceria has shown positive effects on activity and stability for the catalysts used in the reactions discussed above, which often is related to the redox properties of CeO_2. However, ceria is also known for its ability to increase the metal dispersion on the support. Unfortunately, correlations between activity and noble metal dispersion on different supports are often lacking.

The elementary steps involved in steam and CO_2 reforming of methane have been investigated by [47]. Different noble metals (Rh, Ir, Pt, Ru) and support materials (ZrO_2, $\gamma\text{-}Al_2O_3$, $ZrO_2\text{-}CeO_2$) were studied. The results showed that the reforming rates were limited by C-H bond activation and that co-reactant activation was kinetically irrelevant. Furthermore, turnover rates were found to increase with increasing noble metal dispersion. This was related to the presence of coordinatively unsaturated surface metal atoms in catalysts of high metal dispersion, which were more active for C-H bond activation. The support material did not affect turnover rates, except indirectly by influencing the metal dispersion. These conclusions were also valid for $CH_4\text{-}O_2$ reactions, which were found to occur according to the combustion-reforming pathway [48].

Wang et al. [49] investigated the elementary reaction steps in partial oxidation of methane over Rh/Al_2O_3 catalysts. In contrast to the heterogeneous reaction mechanism of Deutschmann used in the present study, a surface reaction scheme including active Al_2O_3 sites for water adsorption was proposed. Inverse spillover of hydroxyls from the support to the metal sites could then occur. The OH spillover effect is, however, dependent on the specific experimental conditions and is expected to be less important at higher temperatures (> 1023 K for alumina) and when high amounts of water are present in the gas phase. Furthermore, it has been shown that dehydroxylation of ZrO_2 is complete at temperatures above 993 K [50]. In the present study, with high amounts of water in the gas phase and catalyst temperatures of 970-1045 K, OH spillover from the support to the metal sites can be considered of minor importance.

In conclusion, the redox properties of ceria appear to be important for certain catalytic systems that are easily deactivated by carbon deposition, which is generally the case for Ni-based catalysts. However, when using Rh this effect should be less significant; the main impact of ceria is to increase the noble metal dispersion, which is in agreement with results of [47]. The numerical predictions presented in the foregoing sections, where no active support sites were included in the surface reaction mechanism, agree well with the experimental results. This indicates that inverse OH spillover from the support can be neglected for most cases studied in the present work. The somewhat worse agreement in H_2 production observed for the catalysts of high Rh dispersion at lower inlet temperature (T_{IN} = 473 K) could potentially be related to water dissociation on support sites. This lower inlet temperature case is, however, not relevant for gas turbine applications where typically T_{IN} > 600 K.

5.4.1 Key conclusions of Section 5.4

a) The Rh dispersion increased in the order Rh/α-Al_2O_3, Rh/ZrO_2 and Rh/Ce-ZrO_2. The Rh/Ce-ZrO_2 catalyst exhibited nearly twice as high dispersion as the Rh/ZrO_2 catalyst. On the other hand, the dispersion of Rh/ZrO_2 was only mildly higher (by 23%) than that of Rh/α-Al_2O_3.

b) The heterogeneous reaction mechanism employed in this study, including only active Rh sites, was able to reproduce with good accuracy experimental results of CPO in exhaust gas-diluted mixtures. The ratio of active to geometrical surface area, deduced from chemisorption analysis, was the single parameter needed in the numerical model to account for the different supports. This indicated that water activation occurring on support sites, resulting in inverse OH spillover from the support to the noble metal sites, could be neglected under the present conditions with high water dilution.

c) An evident relationship between noble metal dispersion and catalytic behavior, in terms of methane conversion and synthesis gas yields, could be established. Both measurements and predictions indicated that an increased Rh dispersion resulted in slightly higher methane conversions, lower surface temperatures and higher synthesis gas yields. It was thus shown that the support material mainly had an indirect effect on the catalytic performance by influencing the noble metal dispersion. The redox properties of ceria, which could prevent catalyst deactivation by carbon deposition, were considered of less importance for Rh-based catalysts and could be excluded in the numerical model, at least under the present conditions with large H_2O dilutions.

6. Schlussfolgerungen

The main conclusions are summarized below separately for each sub-topic.

The conclusions in the topic “validation of hetero-/homogeneous reaction schemes” are:

a) The employed homogeneous reaction scheme, despite deficiencies in the extent of the formaldehyde zone and its propagation characteristics at 10 bar, reproduced well the onset of homogeneous ignition.

b) The heterogeneous reaction scheme provided good agreement to the synthesis gas yields overpredicting slightly the partial over the total oxidation routes. The addition of H_2O increased the CH_4 conversion and H_2 yields and decreased the CO yields, due to a corresponding enhancement in the O(s) and OH(s) surface coverage.

c) An increase in pressure from 4 to 10 bar had a minor effect on the methane conversion and hydrogen selectivity, while the addition of CO_2 had a minimal chemical impact.

The conclusions in the topic “impact of H_2O and CO_2 dilution in CPO of methane” are:

a) The employed catalytic reaction scheme reproduced the measured temperatures along the reactor as well as the measured exit composition, overpredicting mildly the impact of the total over the partial oxidation route. The overprediction was more pronounced at lower inlet temperatures.

b) The reactor thermal management was an important issue in practical reactors. The surface temperatures exceeded by as much as 200 K the adiabatic equilibrium temperature due to the short residence times and the multiple reaction pathways that included complete and total oxidation, steam reforming and water gas shift. It was shown that thermal management approaches solely based on heat transfer mechanisms in the solid substrate were inadequate in controlling the surface temperatures.

c) The presence of H_2O provided a source for surface oxygen and hydroxyl-radicals, O(s) and OH(s), which in turn resulted in higher methane conversion, higher H_2 and lower CO selectivity. This was highly desirable for CPO-based turbine reactors as hydrogen can aid the stabilization of the post-catalyst gaseous combustion zone. The higher hydrogen selectivities were attributed to the more favorable competition of hydrogen desorption ($2H(s) \rightarrow 2Rh(s)+H_2$) over surface oxidation ($H(s)+O(s) \rightarrow Rh(s)+OH(s)$ and $H(s)+OH(s) \rightarrow Rh(s)+H_2O(s)$). On the other hand, the CO selectivity decreased due to the promotion of its surface oxidation ($CO(s)+O(s) \rightarrow Rh(s)+CO_2(s)$).

d) The addition of CO_2 had a minor impact on the CH_4 conversion and the H_2 or CO selectivity during CPO with large H_2O dilution. Therefore, CO_2 reforming is not important in short contact time gas-turbine reactors with exhaust recirculation.

The conclusions in the topic “Ignition and extinction in CPO of methane with large EGR” are:

a) The employed heterogeneous reaction scheme reproduced the measured minimum inlet temperatures required for light-off, the elapsed times for the propagation of the reaction front, and the steady-state exhaust gas compositions in CPO with EGR at a fuel-to-oxygen equivalence ratio $\varphi = 4.0$. At $\varphi = 2.5$, however, only qualitative agreement was obtained and the numerical model overpredicted the synthesis gas yields.

b) The chemical impact of the added H_2O in the feed was already evident at the early stages of the transient catalytic ignition event and its importance further increased as steady state was approached. At steady state, the large H_2O dilution resulted in increased hydrogen selectivity, decreased CO selectivity and slightly increased methane conversion. The chemical impact of CO_2 dilution was minimal on both the transient event and the subsequent steady combustion.

c) Despite the significant chemical impact of H_2O dilution during the light-off process, the ignition delay times themselves were practically unaffected by its presence. The reason was that light-off times were dominated by total oxidation reactions and not by partial oxidation or reforming reactions leading to synthesis gas products. The key reaction affecting catalytic ignition was the surface oxidation of CO to CO_2, which was the main exothermic heat release step in the induction zone. The surface oxidation of H_2 to H_2O, on the other hand, was less significant due to the low amounts of H_2 formed in the induction zone.

d) Measurements and predictions indicated that vigorous combustion could be sustained at inlet temperatures as low as 473 K in CPO with EGR. In CPO without EGR, vigorous combustion was still possible with inlet temperatures as low as 298 K. The reason for the extended stability limits of CPO combustion was the shift from partial to total oxidation products –and hence to higher exothermicity– with decreasing inlet temperature.

e) Computed extinction characteristics obtained at various reactor residence times indicated that extinction in CPO with EGR was possible only at very short times (< 4 ms), which were not relevant to new power generation cycles. On the other hand, in CPO without EGR stable combustion was attained at residence times as short as 1 ms. The key parameter controlling catalytic extinction in CPO was the CO(s) coverage. Near extinction CO(s) increased, reducing the free sites and thus leading to catalyst poisoning.

f) The advantage of reactor materials with high thermal conductivity has been demonstrated for practical CPO systems. Moreover, operation at non-optimal stoichiometries ($\varphi = 2.5$) was shown to be beneficial in CPO with large EGR, due to the moderating effects of dilution on the maximum reactor temperature.

The conclusions in the topic “Effect of catalyst support on the CPO processes” are:

a) The Rh dispersion increased in the order Rh/α-Al_2O_3, Rh/ZrO_2 and Rh/Ce-ZrO_2. The Rh/Ce-ZrO_2 catalyst exhibited nearly twice as high dispersion as the Rh/ZrO_2 catalyst. On the other hand, the dispersion of Rh/ZrO_2 was only mildly higher (by 23%) than that of Rh/α-Al_2O_3.

b) The heterogeneous reaction mechanism employed in this study, including only active Rh sites, was able to reproduce with good accuracy experimental results of CPO in exhaust gas-diluted mixtures. The ratio of active to geometrical surface area, deduced from chemisorption analysis, was the single parameter needed in the numerical model to account for the different supports. This indicated that water activation occurring on support sites, resulting in inverse OH spillover from the support to the noble metal sites, could be neglected under the present conditions with high water dilution.

c) An evident relationship between noble metal dispersion and catalytic behavior, in terms of methane conversion and synthesis gas yields, could be established. Both measurements and predictions indicated that an increased Rh dispersion resulted in slightly higher methane conversions, lower surface temperatures and higher synthesis gas yields. It was thus shown that the support material mainly had an indirect effect on the catalytic performance by influencing the noble metal dispersion. The redox properties of ceria, which could prevent catalyst deactivation by carbon deposition, were considered of less importance for Rh-based catalysts and could be excluded in the numerical model, at least under the present conditions with large H_2O dilutions.

Symbolverzeichnis

B	ratio of active to geometrical surface area
c_p, c	specific heat of gas at constant pressure, specific heat of solid, (J/g K)
D_{km}	mixture-average diffusion coefficient of *k*-th species (m/s)
D_k^T	thermal diffusion coefficient of *k*-th species (m/s)
h	total enthalpy of gaseous mixture (J/g)
h_k , h_k°	total and chemical enthalpy of *k*-th species (J/g)
K_g	total number of gas-phase species
L, L_c, L_u	total reactor length, coated length, uncoated length (m)
M_s	total number of surface species
p	pressure (N/m^2)
$\dot{q}_{\mathrm{acc}}$, $\dot{q}_{\mathrm{gen}}$	heat accumulation and heat generation (W/m^2)
$\dot{q}_{\mathrm{rad}}$, $\dot{q}_{\mathrm{cond}}$, $\dot{q}_{\mathrm{conv}}$	radiative, conductive and convective heat transfer (W/m^2)
Re	Reynolds number
r_h	channel hydraulic radius (m)
$\dot{s}_k$	heterogeneous molar production rate of *k*-th species (gmol/m^{2}s)
S_k	selectivity of *k*-th species
S/V	surface-to-volume ratio
t	time (s)
T	temperature (K)
T_{o}, T_{eq}	reference temperature, adiabatic equilibrium temperature (K)
u, U_{IN}	axial velocity component, inlet axial velocity (m/s)
v	radial velocity component (m/s)
$\vec{V}_k$	diffusion velocity vector of *k*-th gaseous species (m/s)
W_k , $\overline{W}$	species molecular weight, average molecular weight (g/gmol)
X_k, Y_k	gas-phase species mole and mass fraction
x, r	streamwise and radial coordinates

Greek Symbols

α	thermal diffusivity,$\lambda/\rho c$ (m^2/s)
Γ	surface site density (gmol/m^2)
δ, δ_c	channel wall thickness, catalyst layer thickness (m)
ε	surface emissivity
θ_m	surface species coverage
λ	thermal conductivity (W/m K)
μ	viscosity (N m^{-2} s)
ρ	density (g/m^3)
σ_m	surface species site occupancy
τ	reactor residence time (s)

φ	fuel-to-air equivalence ratio
$\dot{\omega}_k$	gas-phase molar production rate of *k*-th species (gmol/m^3 s)

Subscripts

IN, OUT	inlet, outlet
g	gas
FeCr, ZrO_2	solid materials
k, *m*	indices for gas-phase and surface species
W	wall
x, *r*	streamwise and radial components

Abbreviations

CPO	catalytic partial oxidation
EGR	exhaust gas recycle
GHSV	gas hourly space velocity

Referenzen

[1] M. Reinke, J. Mantzaras, R. Schaeren, R. Bombach, A. Inauen, S. Schenker, ***High-pressure catalytic combustion of methane over platinum: In situ experiments and detailed numerical predictions***, Combustion and Flame, 136, 217-240, 2004.

[2] C. Appel, J. Mantzaras, R. Schaeren, R. Bombach, A. Inauen, N. Tylli, M. Wolf, T. Griffin, D. Winkler, R. Carroni, ***Partial catalytic oxidation of methane to synthesis gas over rhodium: in situ Raman measurements and detailed simulations***, Proc. Combust. Inst., 30, 2509-2517, 2005.

[3] C. Appel, J. Mantzaras, R. Schaeren, R. Bombach, A. Inauen, B. Kaeppeli, B. Hemmerling, A. Stampanoni, ***An experimental and numerical investigation of homogeneous ignition in catalytically stabilized combustion of hydrogen/air mixtures over platinum***, Combustion and Flame, 128, 340-368, 2002.

[4] M. Reinke, J. Mantzaras, R. Bombach, S. Schenker, A. Inauen, ***Gas phase chemistry in catalytic combustion of methane/air mixtures over platinum at pressures of 1 bar to 16 bar***, Combust. Flame, 141, 448-468, 2005.

[5] B. Steiner, "Raman spectroscopic investigation of turbulent premixed flames", Dissertation, University of Stuttgart, 2002.

[6] S. Eisenberg, "Raman Spectroscopy in a jet flame", Diploma Thesis, University of Goettingen, Max-Planck-Institut for Fluid Mechanics, 1995.

[7] M. Schaefer, W. Ketterle, J. Wolfrum, ***Saturated 2D-LIF of OH and 2D Determination of Effective Collisional Lifetimes in Atmospheric Pressure Flames***, Appl. Phys. B, 52, 341-346, 1991.

[8] W. Kang, O. Fujita, K. Ito, ***Visualization of formaldehyde distribution above platinum plate by using LIF method***, ASME, 118, 82-87, 1996.

[9] T. Griffin, D. Winkler, M. Wolf, C. Appel, J. Mantzaras, "Staged catalytic combustion method for the advanced zero emissions gas turbine power plant", ASME 2004-54101, 2004.

[10] R. Carroni, T. Griffin, J. Mantzaras, M. Reinke, ***High-pressure experiments and modeling of methane/air catalytic combustion for power generation applications***, Catalysis Today, 83, 157-170, 2003.

[11] A. Schneider, J. Mantzaras, P. Jansohn, ***Experimental and numerical investigation of the catalytic partial oxidation of CH_4/O_2 mixtures diluted with H_2O and CO_2 in a short contact time reactor***, Chemical Engineering Science, 61, 4634-4646, 2006.

[12] J. M. Gatica, R. T. Baker, P. Fornasiero, S. Bernal, G. Blanco, J. Kaspar, ***Rhodium dispersion in a $Rh/Ce_{0.68}Zr_{0.32}O_2$ catalyst investigated by HRTEM and H_2 chemisorption***, Journal of Physical Chemistry B, 104, 4667-4672, 2000.

[13] R. J. Kee, G. Dixon-Lewis, J. Warnatz, M. E. Coltrin, J. A. Miller, ***A Fortran computer code package for the evaluation of gas-phase multicomponent transport properties***, Report No. SAND86-8246, Sandia National Laboratories, Report No. SAND86-8246, 1996a.

[14] R. Siegel, J. R. Howell, ***Thermal radiation heat transfer***, Hemisphere, New York, p. 271, 1981.

[15] S. Karagiannidis, J. Mantzaras, G. Jackson, K. Boulouchos, ***Hetero-/homogeneous combustion and stability maps of methane-fueled catalytic microreactors***, Proc. Combust. Instit., 31, 2007, in press.

[16] A. Schneider, J. Mantzaras, S. Eriksson, ***Ignition and extinction in catalytic partial oxidation of methane/oxygen mixtures with large H_2O and CO_2 dilution***, Combustion Science Technology, submitted, 2006.

[17] S. Patankar, ***Numerical heat transfer and fluid flow***, Hemisphere, New York, 131, 1980.

[18] U. Dogwiler, P. Benz, J. Mantzaras, ***Two-dimensional modelling for catalytically stabilized combustion of a lean methane-air mixture with elementary homogeneous and heterogeneous chemical reactions***, Combustion and Flame, 116, 243-258, 1999.

[19] J. Mantzaras, C. Appel, P. Benz, U. Dogwiler, ***Numerical modelling of turbulent catalytically stabilized channel flow combustion***, Catal. Today, 53, 3-17, 2000.

[20] J. H. Ferziger, M. Petric, ***Computational methods for fluid dynamics***, Springer Verlag, New York, p.142, 1999.

[21] R. Schwiedernoch, S. Tischer, C. Correa, O. Deutschmann, ***Experimental and numerical study on the transient behavior of partial oxidation of methane in a catalytic monolith***, Chemical Engineering Science, 58, 633-642, 2003.

[22] A. Schneider, J. Mantzaras, R. Bombach, S. Schenker, N. Tylli, P. Jansohn, ***Laser induced fluorescence of formaldehyde and Raman measurements of major species during partial catalytic oxidation of methane with large H_2O and CO_2 dilution at pressures up to 10 bar***, Proceedings Combustion Institute, 31, 2007, in press.

[23] J. Warnatz, R. W. Dibble, U. Maas, ***Combustion, Physical and Chemical Fundamentals, Modeling and Simulation***, Springer-Verlag, New York, 1996.

[24] M. E. Coltrin, R. J. Kee, F. M. Rupley, ***Surface Chemkin: A Fortran package for analyzing heterogeneous chemical kinetics at the solid surface-gas phase interface***, Report No. SAND90-8003C, Sandia National Laboratories, 1996.

[25] R. J. Kee, F. M. Rupley, J. A. Miller, ***Chemkin II: A Fortran chemical kinetics package for the analysis of gas-phase chemical kinetics***, Report No. SAND89-8009B, Sandia National Laboratories, 1996b.

[26] Z. Hy, ***$CeO_{1.5}$-stabilized tetragonal ZrO_2***, Journal of Materials Science, 29, 4351-4356, 1994.

[27] V. R. Mastelaro, V. Briois, D. P. F. De Souza, C. L. Silva, ***Structural studies of a ZrO_2-CeO_2 doped system***, Journal of the European Ceramic Society, 23, 273-282, 2003.

[28] S. Eriksson, A. Schneider, J. Mantzaras, M. Wolf, S. Jaras, ***Experimental and numerical investigation of supported rhodium catalysts for partial oxidation of methane in exhasut gas diluted reaction mixtures***, Chemical Engineering Science, submitted, 2006.

[29] D. I. Shin, T. Dreier, J. Wolfrum, ***Spatially resolved absolute concentration and fluorescence-lifetime determination of H2CO in atmospheric-pressure CH4/air flames***, Appl. Phys. B, 72, 257-261, 2001.

[30] M. F. Mark, W. F. Maier, ***CO_2-reforming of methane on supported Rh and Ir catalysts***, Journal of Catalysis, 164, 122-130, 1996.

[31] G. Veser, J. Frauhammer, ***Modelling steady state and ignition during catalytic methane oxidation in a monolith reactor***, Chemical Engineering Science, 55, 2271-2286, 2000.

[32] M. F. Mark, W. F. Maier, ***CO_2-reforming of methane on supported Rh and Ir catalysts***, Journal of Catalysis, 164, 122-130, 1996.

[33] R. Schwiedernoch, S. Tischer, C. Correa, O. Deutschmann, ***Experimental and numerical study on the transient behavior of partial oxidation of methane in a catalytic monolith***, Chemical Engineering Science, 58, 633-642, 2003.

[34] E. P. J. Mallens, J. H. B. J. Hoebink, G. B. Marin, ***The reaction mechanism of the partial oxidation of methane to synthesis gas: A transient kinetic study over rhodium and a comparison with platinum***, Journal of Catalysis, 167, 43-56, 1997.

[35] O. V. Buyevskaya, D. Wolf, M. Baerns, ***Rhodium-catalyzed partial oxidation of methane to CO and H_2 – transient studies on its mechanism***, Catalysis Letters, 29, 249-260, 1994.

[36] D. A. Hickman, L. D. Schmidt, ***Production of syngas by direct catalytic oxidation of methane***, Science, 259, 343-346, 1993.

[37] M. Huff, L. D. Schmidt, ***Mechanism of Olefin Production on Pt, Rh, and Pd Catalysts***, Abstracts of Papers of the American Chemical Society, 209, 43-COLL, 1995.

[38] K. Otsuka, Y. Wang, E. Sunada, I. Yamanaka, ***Direct partial oxidation of methane to synthesis gas by cerium oxide***, Journal of Catalysis, 175, 1998.

[39] M. Fathi, E. Bjorgum, T. Viig, O. A. Rokstad, ***Partial oxidation of methane to synthesis gas: elimination of gas phase oxygen***, Catalysis Today, 63, 489-497, 2000.

[40] J. G. Xu, G. F. Froment, ***Methane steam reforming, methanation and water-gas shift: I. Intrinsic kinetics***, AIChE Journal, 35, 88-96, 1989.

[41] S. M. Stagg, E. Romeo, C. Padro, D. E. Resasco, ***Effect of promotion with Sn on supported Pt catalysts for CO_2 reforming of CH_4***, Journal of Catalysis, 178, 137-145, 1998.

[42] W. S. Dong, H. S. Roh, K. W. Jun, S. E. Park, Y. S. Oh, ***Methane reforming over Ni/Ce-ZrO2 catalysts: effect of nickel content***, Applied Catalysis A, 226, 63-72, 2002.

[43] N. Laosiripojana, W. Sutthisripok, S. Assabumrungrat, ***Synthesis gas production from dry reforming of methane over CeO_2-doped Ni/Al_2O_3: influence of the doping ceria on the resistance toward carbon formation***, Chemical Engineering Journal, 112, 13-22, 2005.

[44] N. Laosiripojana, S. Assabumrungrat, ***Methane steam reforming over $Ni/Ce\text{-}ZrO_2$ catalyst: influence of $Ce\text{-}ZrO_2$ support on reactivity, resistance towrad carbon formation, and intrinsic reaction kinetics***, Appl. Catal. A, 290, 200-211, 2005a.

[45] S. Kurungot, T. Yamaguchi, ***Stability improvement of $Rh/\gamma\text{-}Al_2O_3$ catalyst layer by ceria doping for steam reforming in an integrated catalytic membrane recator system***, Catalysis Letters, 92, 181-187, 2004.

[46] F. B. Passos, E. R. De Oliveira, L. V. Mattos, F. B. Noronha, ***Partial oxidation of methane to synthesis gas on $Pt/Ce_xZr_{1-x}O_2$ catalysts: the effect of the support reducibility and of the metal dispersion on the stability of the catalysts***, Catalysis Today, 101, 23-30, 2005.

[47] J. Wei, E. Iglesia, ***Mechanism and site requirements for activation and chemical conversion of methane on supported Pt clusters and turnover rate comparisons among noble metals***, Journal of Physical Chemistry B, 108, 4094-4103, 2004.

[48] E. Iglesia, "Kinetic coupling and methane activation on supported metal clusters: structural requirements and reaction pathway", 12th Nordic Symposium on Catalysis, Trodheim, Norway, 2006.

[49] D. Wang, O. Dewaele, A. M. De Groote, G. F. Froment, ***Reaction mechanism and role of the support in the partial oxidation of methane on Rh/Al_2O_3***, Journal of Catalysis, 159, 418-426, 1996.

[50] K. Stoppek-Langner, J. Goldwasser, M. Houalla, D. M. Hercules, ***Infrared and carbon-dioxide chemisorption study of Mo/ZrO_2 catalysts***, Catalysis Letters, 32, 263-271, 1995.